# MAPPING OF ALTERATION ZONES IN NORTH GHOUBBET (TADJOURA, DJIBOUTI)

## using Worldview-3 high resolution Satellite Imagery

Hannover, November 2021


| | |
|---|---|
| Author | Alina Ermertz<br>Federal Institute for Geosciences and Natural Resources<br>(BGR), Remote Sensing Unit |
| Commissioned by: | Federal Ministry for Economic Cooperation and Development (Bundesministerium für wirtschaftliche Zusammenarbeit und Entwicklung, BMZ) |
| Project | Regional Project Geothermal Energy East Africa |
| BMZ Number: | 2016.2066.5 |
| BGR Number: | 05-2392 |
| Pages | 40 |
| Place and date of issue | Hannover, November 2021 |

To be cited as: Ermertz (2021): Mapping of Alteration Zones in North Ghoubbet (Tadjoura, Djibouti) using Worldview-3 high resolution Satellite Imagery, BGR project number 05-2393, Hannover.

# Table of Contents

**Abbreviations**
**List of figures**
**Summary**

# Abbreviations

| | |
|---|---|
| BGR | Bundesanstalt für Geowissenschaften und Rohstoffe (Federal Institute for Geosciences and Natural Resources) |
| ODDEG | Office Djiboutien de Développement de l'Énergie Géothermique |
| PC | Principal Component |
| PCA | Principal Component Analysis |
| RGB | Red Green Blue (colour band combination) |
| SAM | Spectral Angle Mapper |
| SRTM | Shuttle Radar Topography Mission |
| SWIR | Short Wavelength Infrared |
| USGS | United States Geological Survey |
| VNIR | Visible and Near-Infrared |
| WP | Waypoint (measured by GPS) |
| WV-3 | Worldview-3 |

# List of figures

# Summary

The technical cooperation project “Geothermal Energy in East Africa” includes cooperation with the Djiboutian project partner *Office Djiboutien de Développement de l’Énergie Géothermique* (ODDEG). Several remote sensing methods are applied to provide support for current geothermal exploration studies.

Focus of these studies is the area *North Ghoubbet* in central Djibouti, where freely available multispectral satellite imagery and digital elevation models were already used for lineament analysis to assess the tectonic framework of the site (Ermertz 2020). In this study, high-resolution Worldview-3 (WV-3) data are used for the mapping of hydrothermal alteration zones, considered as surface indicators for hydrothermal activity. Field investigations in context of lineament mapping studies showed that geothermal manifestations, mainly fumaroles, are associated with the occurrence of alteration zones with a few meters of extension. Alteration minerals primarily consist of iron-bearing minerals and clay minerals. The high spatial and spectral resolution of the WV-3 imagery (1.6 m – 3.7 m) enables the mapping of locations where these mineral assemblages occur.

The combination of different image processing and information extraction techniques like band ratioing, spectral angle mapping and principal component analysis allows the assessment of areas where the alteration footprints and thus hydrothermal activity is particularly high. In case of *North Ghoubbet*, especially the southern part of the study area is characterized by high alteration mineral occurrences and can be defined as the center of hydrothermal activity that most probably correlates with the existence of a wide fault zone facilitating fluid flow by structures extending to high depth.

Several locations with increased occurrences of alteration minerals are defined that should be part of upcoming field investigations.

# 1 Scope of the Work

This report is part of a remote sensing study that includes the application of several remote sensing methods to support the exploration of the geothermal site *North Ghoubbet* in central Djibouti. Lineament mapping was already conducted based on multispectral and digital elevation data (see report Lineament Analysis: Ermertz 2020). This study focusses on the application of high-resolution multispectral data for the mapping of alteration zones.

The evidence for a geothermal system often is provided by surface expressions like hot springs, fumaroles or geysers. Another, even more common feature is the occurrence of alteration zones, as a result of an interaction between the host rock and hydrothermal fluids (Abubakar et al. 2019). Hence, the occurrence of altered material indicates locations of fluid flow in a geothermal reservoir (Abhary & Hassani 2016). Resulting geothermal-related alteration minerals include clays, carbonates, silicates and calcites (Abubakar et al. 2019, Browne 1978, Calvin et al. 2015). Each mineral, or each mineral group, has a characteristic spectral reflectance feature measurable with sensors of an adequate spectral resolution.

Sensors carried by the Worldview-3 (WV-3) satellite are capable of identifying spectral patterns of these mineral groups and enable mapping mineral assemblages (Kruse et al. 2015). The WV-3 data include high-resolution visible near infrared (VNIR) and short wavelength infrared (SWIR) imagery, both used in this study to map the locations of altered rocks characterized by specific alteration mineral assemblages. Locating these alteration zones leads to the definition of hydrothermally active zones and supports the characterization of the geothermal system.

# 2 Geothermal Exploration in the Republic of Djibouti

The history of geothermal exploration in Djibouti began in the 1970's. Since then, exploration studies were conducted at different sites and in cooperation with several counterparts from France, Italy and Turkey (Aden et al. 2018, Zan et al. 1990). Exploration studies focused on the central part of the Asal-Ghoubbet rift, benefitting from a shallow heat source as indicated by the location of the recently active Fieale volcano in the center of the rift. As this rift is located in between Lac Asal and Lac Ghoubbet, the latter one being connected to the sea, the fluids of the geothermal reservoir are characterized by a high salinity, leading to mineral scaling and corrosion of the drilling equipment (Aden et al. 2018, Houssein & Axelsson 2010).

The study area *North Ghoubbet* is currently subject to investigation, as it is thought to be a promising site benefiting from the shallow heat source of the Asal-Ghoubbet rift system and a reservoir that is fed by meteoric waters from the Goda Mountains rather than saline waters from the sea (Varet 2010).

# 3 Working Area

The Republic of Djibouti is part of the Horn of Africa in Eastern Africa. The working area *North Ghoubbet* is located in the central part of the country, in the southern region of Tadjoura. The area of *North Ghoubbet* is bordered by Lake Ghoubbet to the south and the Asal-Ghoubbet rift system to the southwest.

The WV-3 imagery acquired for this investigation covers 101 km² in the area of *North Ghoubbet*. The same area, slightly larger, was also used for the lineament analysis described in *Ermertz 2020*. The highest elevations of approximately 575 m above sea level are reached in the central part. The Goda Mountain Range lies a few kilometers north of the study area, and run off water from these mountains feed North Ghoubbet with meteoric waters. The extensive wadi systems Wadi Afay and Wadi Analé occur in the central part and are easily visible on the satellite imagery (Figure 3.1b).

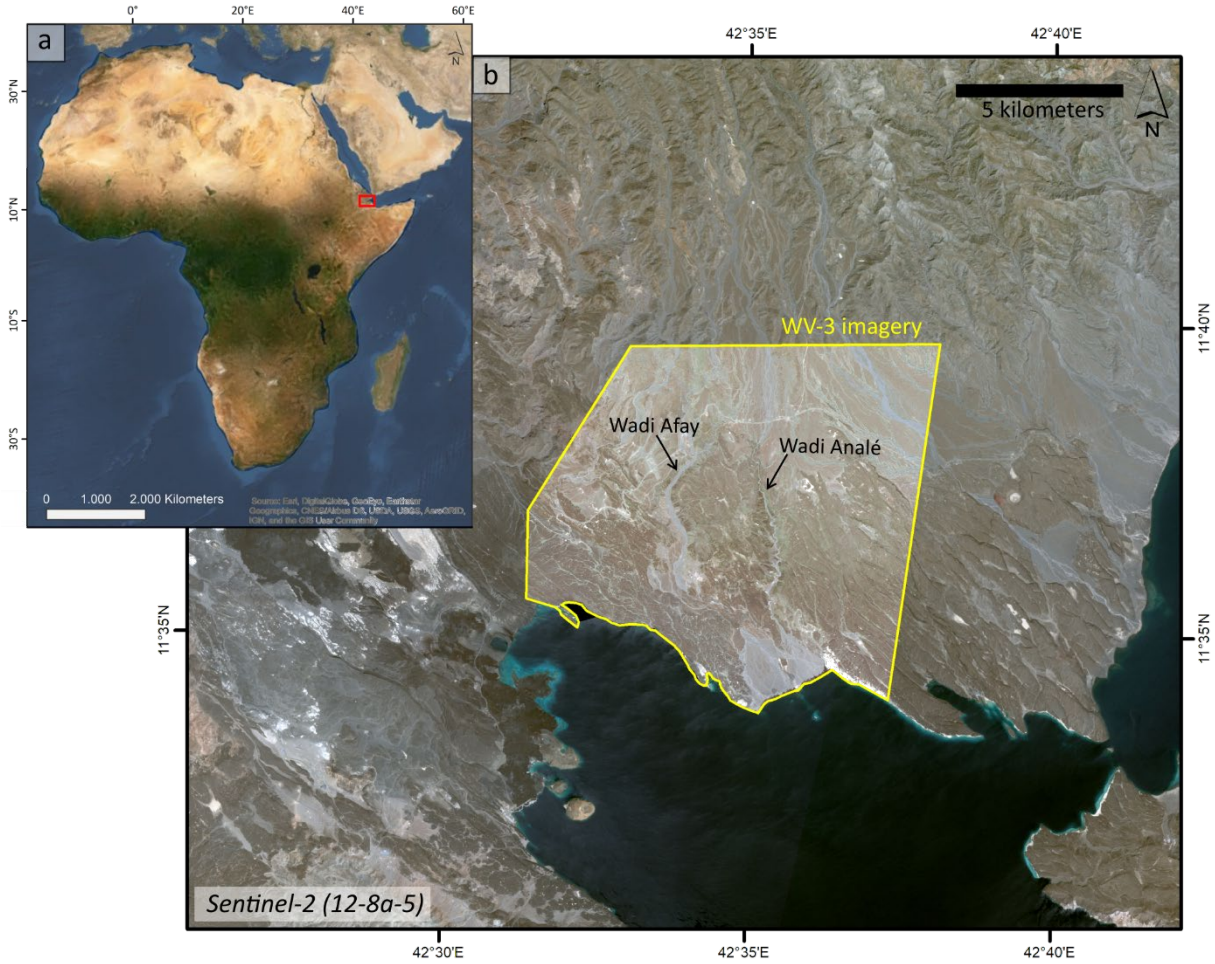


*Figure 3.1: (a) Red rectangle represents the location of Djibouti on the African continent. (b) Extent of the working area North Ghoubbet in central Djibouti, corresponding to the extent of the WV-3 imagery. Displayed on a Sentinel 2A scene from 23.10.2019, bands 12-8a-5 (RGB). Contains modified Copernicus Sentinel data [2019].*

# 4 Geology & Plate Tectonic Setting

Djibouti is located in East Africa being part of the Afar region. This region is known for its unique geological setting, as the two spreading ridges of the Red Sea and the Gulf of Aden meet the East African Rift System and form a huge depression, the Afar Triple Junction (Chorowicz 2005). Continental rifting started in Oligocene times and has been ongoing since, resulting in major tectonic and volcanic activities.

The most recent geological units of the Afar Triangle and the region of Djibouti are volcanic rocks resulting from active rifting, overlying the Neoproterozoic basement and partly Mesozoic sedimentary rocks (Beyene & Abdelsalam 2005). Figure 4.1a shows a simplified geological map of the area. Basalts of the Stratoid Series of Pliocene-Pleistocene age cover most of the Djiboutian territory (Vellutini 1990). Approximately, at the same time, basalts indicated as Basalts of the Gulf in Figure 4.1a erupted during the opening of the Gulf of Tadjoura which represents the western elongation of the Gulf of Aden.

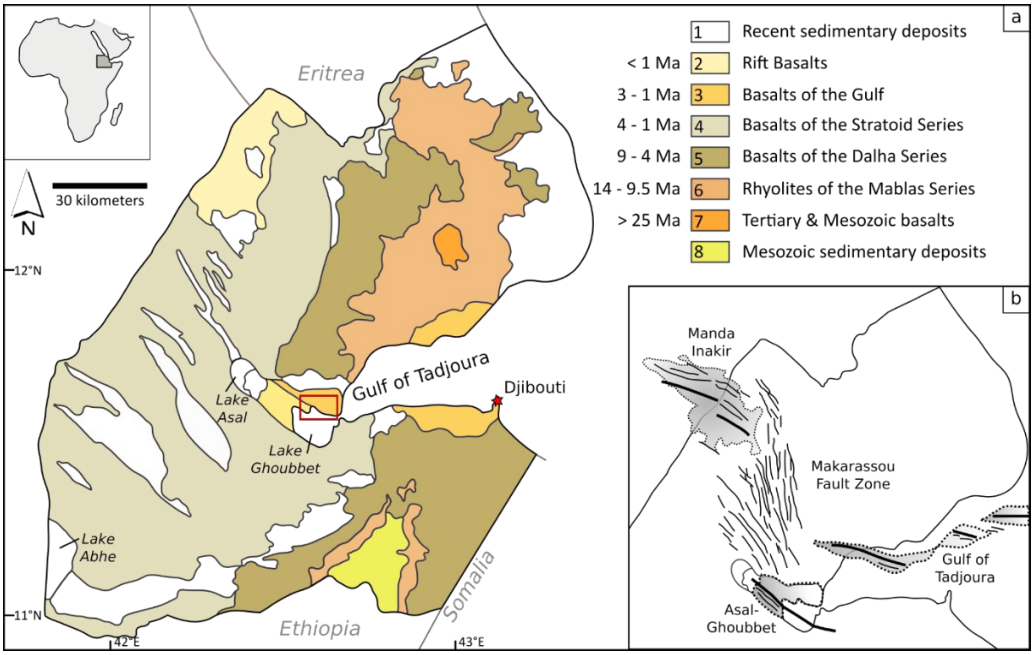


*Figure 4.1: (a) Simplified geological map of the Republic of Djibouti (modified after Vellutini 1990). The red rectangle shows the location of the study area. (b) Major geological structures controlling the tectonic framework of the area: the Manda Inakir Rift in the north, the Asal-Ghoubbet Rift in the south, both oriented NW-SE and the N(NW)-S(SE) trending Makarassou Fault Zone connecting both (modified after Vellutini 1990).*

The youngest deposits of Djibouti are Rift Basalts that erupted in the two rift systems Manda Inakir and Asal-Ghoubbet in different phases throughout the Quaternary (de Chabalier & Avouac 1994). The red rectangle in Figure 4.1a shows the location of the study area North Ghoubbet that consists of two main rock groups from the geological units described above. The Basalts of the Gulf occur in the northeastern part and the Rift Basalts of the Asal Rift occur in a small part in the southwest (Figure 4.1a).

The tectonic framework of North Ghoubbet is influenced by major geological structures as indicated in Figure 4.1b. The two rift systems Manda Inakir and Asal-Ghoubbet are both trending NW-SE, while the N(NW)-S(SE) trending Makarassou Fault Zone acts as a transfer zone between them (Le Gall et al. 2011, Polun et al. 2018, Vellutini 1990).

Figure 4.2 shows the result from lineament analysis. Most of the lineaments are oriented 300° NW-SE, corresponding to the Asal-Ghoubbet Rift trend (Ermertz 2020). Conjugated structures appear in a 45° NE-SW orientation, visible on the rose diagram in Figure 4.2a. As the Asal-Ghoubbet Rift system is located close to the study area, it majorly influences the tectonic directions. The major 300° NW-SE orientation develops to a more northerly trend of 315°NW-SE towards the northern part of the study area, indicating an increasing influence of the Makarassou Fault Zone towards the north(west). Different features like right stepping segmentation, pull-apart structures and horsetail structures can be observed in the mapped lineaments and indicate a sinistral direction of shear.

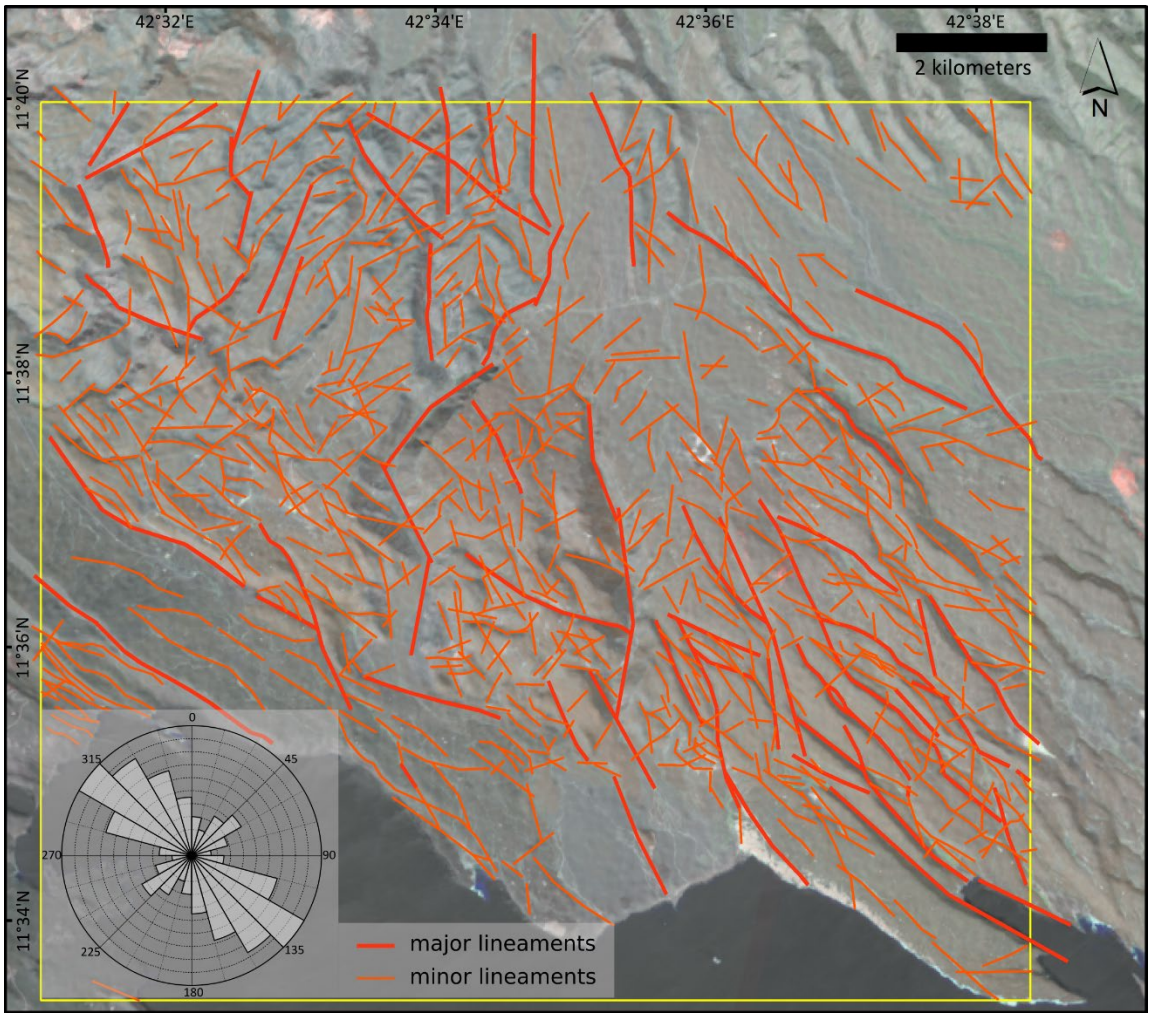


*Figure 4.2: Lineaments in the study area of North Ghoubbet. Background: Sentinel-2 scene (bands 12-8a-5), transparent on shaded relief map (SRTM).*

*For a more detailed description of the geological and tectonic history and the lineament analysis, please see the report "Lineament Mapping in North Ghoubbet (Tadjoura, Djibouti)" (Ermertz 2020).*

# 5 Mineral Mapping

## 5.1 Minerals in geothermal systems

The circulation of hydrothermal fluids in a geothermal system is often accompanied by hydrothermal alteration of the host rock. During this process, the mineralogy and chemistry of the host rock, in this case basalt, is altered by interacting with hydrothermal fluids. Important factors on which alteration processes depend on are temperature and the chemical composition of the fluid and the host rock (Berger 1998). In geothermal context, the occurrence of altered material is a surface indicator for geothermal activity and indicates the locations of fluid flow in a geothermal reservoir. The most common minerals associated with hydrothermal alteration are carbonates, sulfates, iron bearing minerals and clay minerals (Abhary & Hassani 2016, Calvin et al. 2015, Sun et al. 2017).

There are different types of alteration depending on the host rock, the chemistry of the hydrothermal fluid, and the temperature at which the alteration takes place. Each alteration type results in characteristic alteration products (Brown et al. 2005, Mathieu 2018, Sun et al. 2017). Argillic and propylitic alteration types are typical for geothermal environments (Abubakar et al. 2019, Teklemariam et al. 1996). Argillic alteration mainly produces clay minerals, dominated by kaolinite and smectite minerals (montmorillonite, illite), while products of propylitic alteration are carbonates and, to a certain extent, chlorite (Calvin et al. 2015, Kruse et al. 2015, Mas et al. 2006).

Figure 5.1 shows examples for alteration zones in North Ghoubbet that mostly have an extension of several meters. The predominant alteration types are argillic and propylitic with the main alteration minerals clay, carbonates and iron oxides/hydroxides.

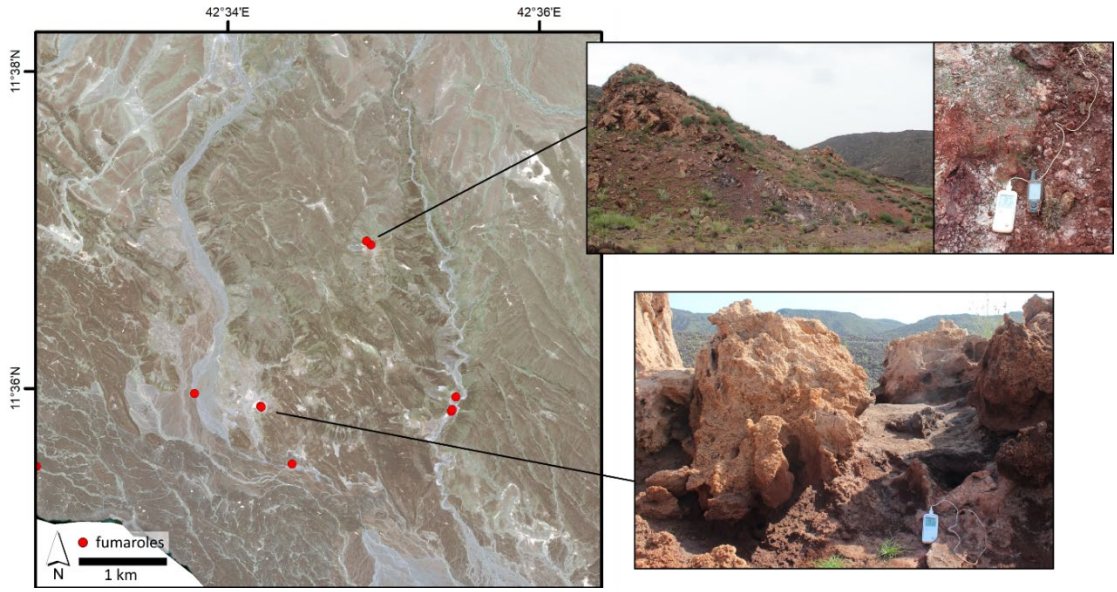


*Figure 5.1: Alteration zones in North Ghoubbet. The map shows locations of fumaroles that often correlate with alteration zones, as shown in the pictures on the right.*

## 5.2 Worldview-3 Data

Worldview-3 (WV-3) data form the basis for mapping alteration zones in *North Ghoubbet*. The WV-3 satellite was launched in August 2014 and is equipped with a sensor recording 16 bands in the visible and near-infrared (VNIR) and short wavelength infrared (SWIR) region of the electromagnetic spectrum. The WV-3 bands with their corresponding spectral band range are listed in Table 1**.** The VNIR bands with a spatial resolution of 1.6 meters and the SWIR bands with a spatial resolution of 3.7 meters were recorded on May 10th 2020**.** The data was delivered by DigitalGlobe in the Product Level LV3D (DigitalGlobe 2014), including an atmospheric compensation (AComp) and an orthorectification based on Shuttle Radar Topography Mission (SRTM) digital elevation data.

*Table 1: Table showing the spectral bands of WV-3 VNIR and SWIR sensor.*

| | **WV-3 Bands** | **Spectral band range [nm]** |
|---|---|---|
| VNIR (1.6m) | B1: Coastal blue | 400 – 450 |
| | B2: Blue | 450 – 510 |
| | B3: Green | 510 – 580 |
| | B4: Yellow | 585 – 625 |
| | B5: Red | 630 – 690 |
| | B6: Red edge | 705 – 745 |
| | B7: Near-Infrared 1 | 770 – 895 |
| | B8: Near-Infrared 2 | 860 – 1040 |
| SWIR (3.7m) | B9: SWIR-1 | 1195 – 1225 |
| | B10: SWIR-2 | 1550 – 1590 |
| | B11: SWIR-3 | 1640 – 1680 |
| | B12: SWIR-4 | 1710 – 1750 |
| | B13: SWIR-5 | 2145 – 2185 |
| | B14: SWIR-6 | 2185 – 2225 |
| | B15: SWIR-7 | 2235 – 2285 |
| | B16: SWIR-8 | 2295 – 2365 |

As part of the preprocessing, the SWIR bands were resized to 1.6 meters, so all bands have the same resolution. The resampled bands were stacked into one single file providing a 16-band data cube. Preprocessing steps, image processing/enhancement and information extraction was conducted in ENVI Version 5.5.3 and ERDAS 2020. Results are imported into ArcMap version 10.3.1 for further interpretation and comparison with additional data (e.g. lineaments, topography).

For all data, the spatial reference system UTM 38 N, WGS 84 is used.

## 5.3 Mineral Spectroscopy Overview (Spectral Reflectance Curves)

Optical remote sensing systems like the WV-3 satellite sensor measure the reflectance of electromagnetic energy by an object. The recorded reflectance can be visualized as a function of the wavelength, resulting in a graph called spectral reflectance curve, as shown in Figure 5.2 (Lillesand et al. 2008). The spectral reflectance curves show features that are characteristic for different materials, like the laboratory spectral reflectance curves of water, vegetation and dry bare soil in Figure 5.2, allowing to distinguish materials based on their reflectance characteristics. Spectral characteristics of different mineral groups are based on their chemical and mineralogical composition, as specific ion complexes result in unique and diagnostic spectral absorption features. However, the ability to define single minerals or even mineral groups depends on the spectral and spatial resolution of the data.

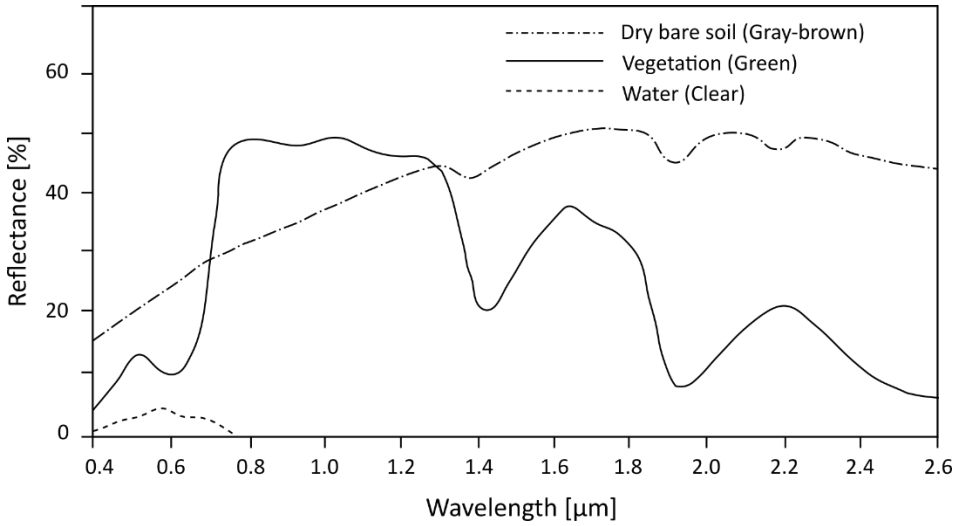


*Figure 5.2: Spectral reflectance curve of dry bare soil, vegetation and water (Lillesand et al. 2008).*

The commercial WV-3 satellite system currently is the multispectral satellite with the highest spatial and spectral resolution, delivering data in the VNIR and SWIR range, as described in chapter 5.2. The spectral and spatial resolution of the WV-3 data enables mapping mineral assemblages. Several studies showed that WV-3 data is well suited for mineral mapping, although in most cases it was combined with hyperspectral airborne, field and laboratory data, to calibrate and validate spaceborne data (Karimzadeh & Tangestani 2019, Kruse et al. 2015, Mars 2018).

In terms of this study, WV-3 data is applied for the mapping of alteration mineral assemblages. Although there has not been a detailed study of the alteration zones and their containing minerals so far, it is known from a brief field inspection that clay minerals and iron bearing minerals are characteristic for these alteration zones in North Ghoubbet (see chapter 5.1). So-called spectral libraries, as for example the United States Geological Survey (USGS) spectral

library, contain reference data for minerals, mineral mixtures, rocks, soils and different types of vegetation measured in the laboratory (Kokaly et al. 2017).

Spectral reflectance curves of minerals that are relevant in this study are shown in Figure 5.3, assorted by Al-OH bearing minerals, carbonates and iron bearing minerals with their characteristic spectral absorption features. These curves were resampled from the original spectral resolution of the USGS library to the WV-3 band resolution. Both curves, original USGS and resampled to WV-3, are shown in Figure 5.3.

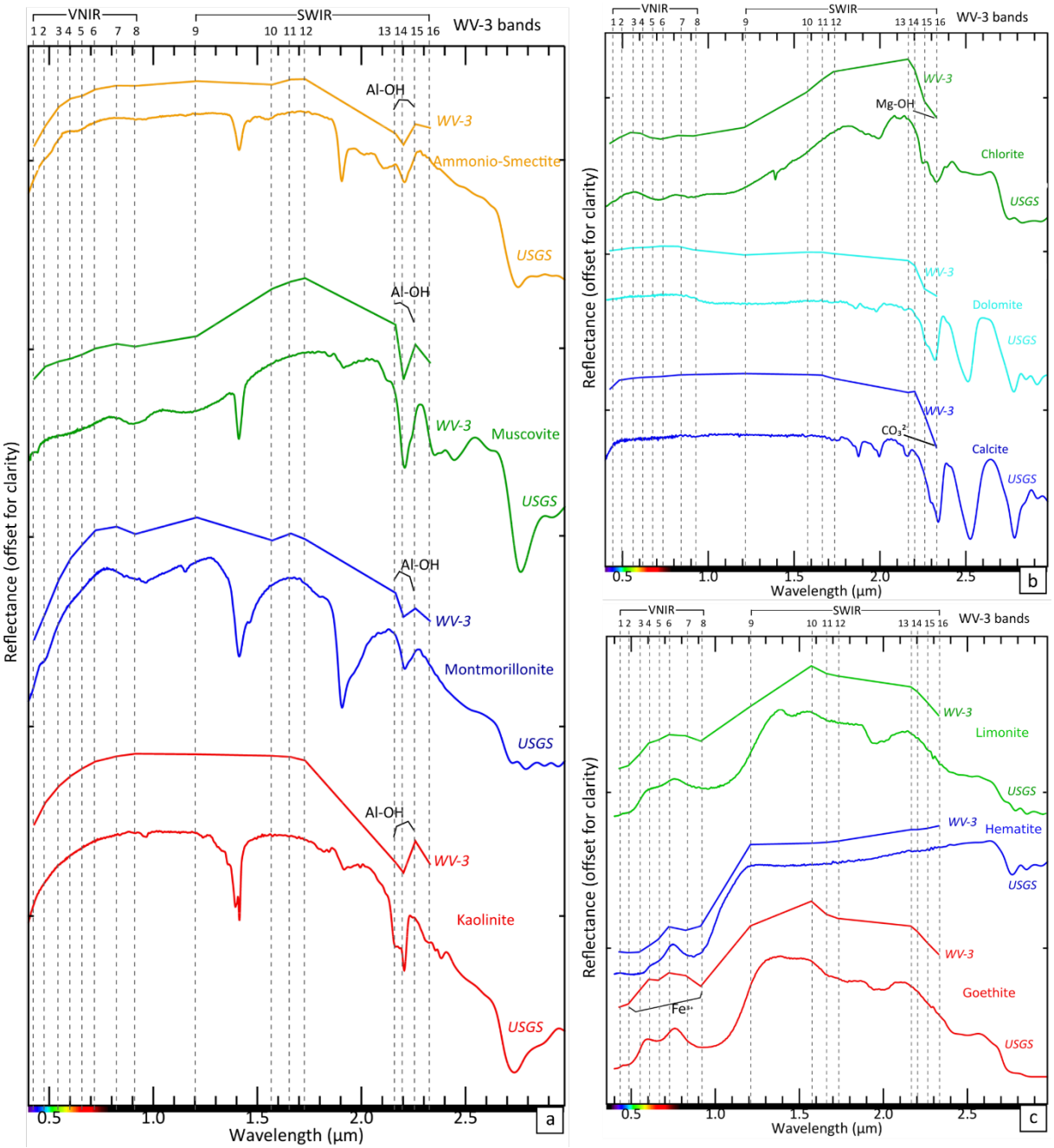


*Figure 5.3: Spectral reflectance curves for selected minerals, each showing a pair of USGS spectral library sample data and resampled spectra for the WV-3 bands. (a) Al-OH bearing minerals kaolinite, muscovite and montmorillonite (argillic alteration minerals), characterized by the Al-OH feature. (b) Carbonate minerals and chlorite (propylitic alteration minerals) with overlapping spectral absorption features in SWIR band 8. (c) Iron bearing minerals goethite, hematite and limonite with absorption features in the VNIR range.*

Mineral representatives for argillic alteration processes are clay minerals including assemblages of kaolinite, muscovite and montmorillonite. These Al-OH bearing minerals share a characteristic absorption feature in the SWIR wavelength region ranging from approximately 2.17 µm to 2.2 µm (Mars 2018, Sun et al. 2017). This wavelength range is covered by WV-3 SWIR bands 13, 14, and 15 (Figure 5.3a).

An additional mineral group of interest are evaporates and chemical precipitates like calcite and dolomite as the location of these minerals might indicate upwelling geothermal fluids (Kratt et al. 2010). The characteristic absorption features for calcite and dolomite appear between 2.3 and 2.35 µm, covered by SWIR band 16 (Kruse et al. 2015, Figure 5.3). These carbonates occur along with minerals containing a Mg-OH complex (e.g. chlorite, epidote, serpentine) in propylitic alteration environments. As the Mg-OH bearing minerals show a characteristic absorption at wavelength of 2.30 – 2.40 µm, as well covered by SWIR band 16, they are not easily distinguishable from the carbonate minerals in the WV-3 data set (Sun et al. 2017).

The iron bearing minerals goethite, hematite and limonite show characteristic absorption features related to $Fe^{2+}$ /$Fe^{3+}$ at wavelengths of approximately 0.49, 0.7 and 0.85 µm range (Mars 2018, Sun et al. 2017), which is covered by the WV-3 VNIR bands 2, 5, 6, 7 and 8 (Figure 5.3c).

## 5.4 Information Extraction Techniques

There are different methods to extract information from remote sensing data. It is possible to enhance specific features by simply combining different bands forming false color compositions. Band ratios support the enhancement of characteristic spectral absorption features while classification methods help discovering areas of high spectral similarity. Principal Component Analysis is a statistical method to extract information from a multispectral data set. The different methods are described in the following.

The image processing was conducted on the entire WV-3 scene. Detailed examination is focused on the areas of interest that were already defined based on the results of the lineament analysis (Figure 5.4). The minerals that were chosen for further analysis with the methods mentioned above are the ones that are known to be very common in geothermal environments, as described in chapter 5.1. Due to a lack of detailed geochemical or mineralogical information, the analysis is focused on mineral groups rather than specific minerals. Locations where alteration or fumarolic activity are documented from field investigations are displayed in Figure 5.4. These locations are taken as reference points for the assessment of the resulting maps.

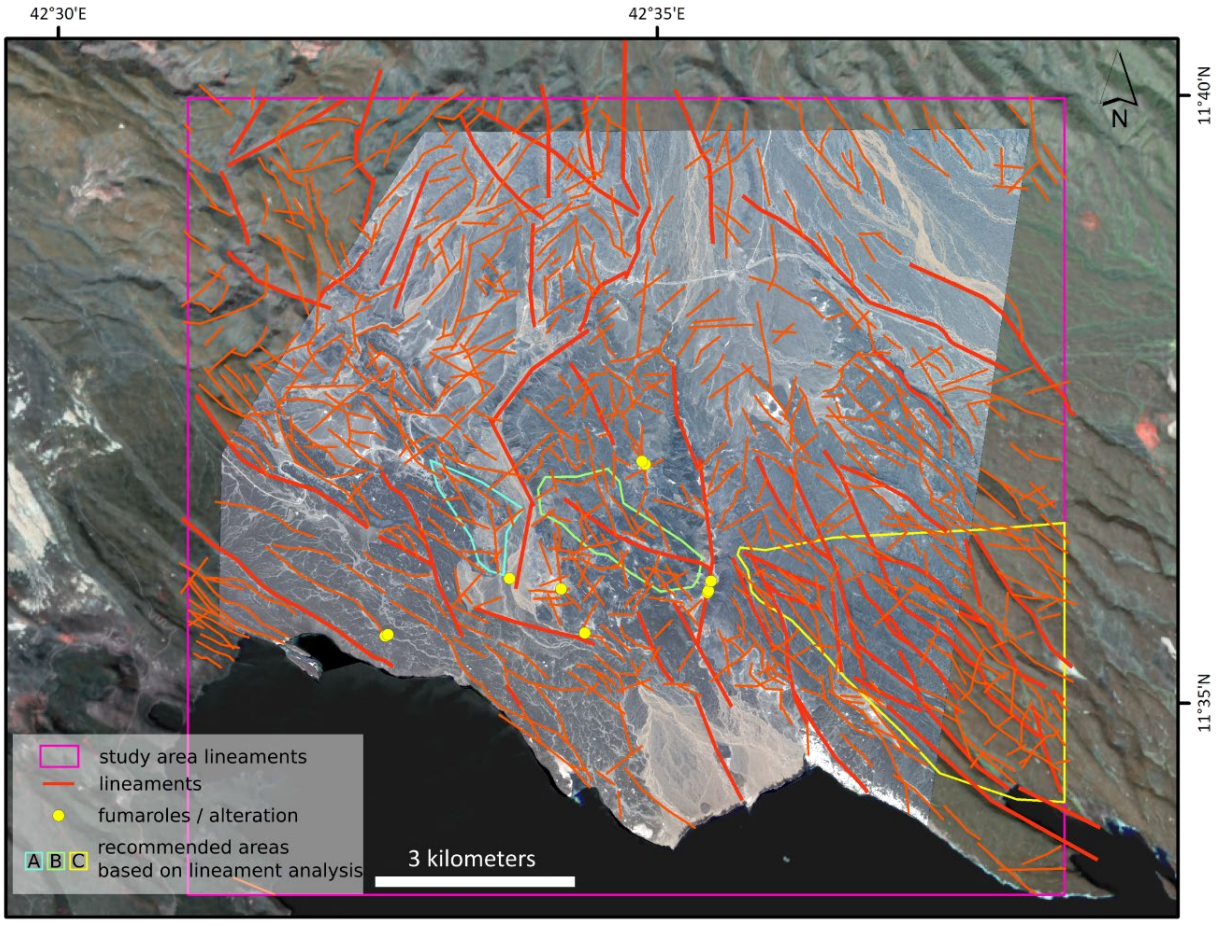


*Figure 5.4: Results of the lineament analysis based on Sentinel-2 and SRTM data (contains modified Copernicus Sentinel data [2020]). Three polygons show the areas that were defined for further analysis based on the lineament analysis. A true color composite of the WV-3 scene (bands 5-3-2) is displayed as well.*

### 5.4.1 Color and false color composites

A simple way to visualize the occurrence of specific materials is generating color composites by selecting three bands for the RGB display based on spectral features of the specific materials, as shown in Figure 5.5.

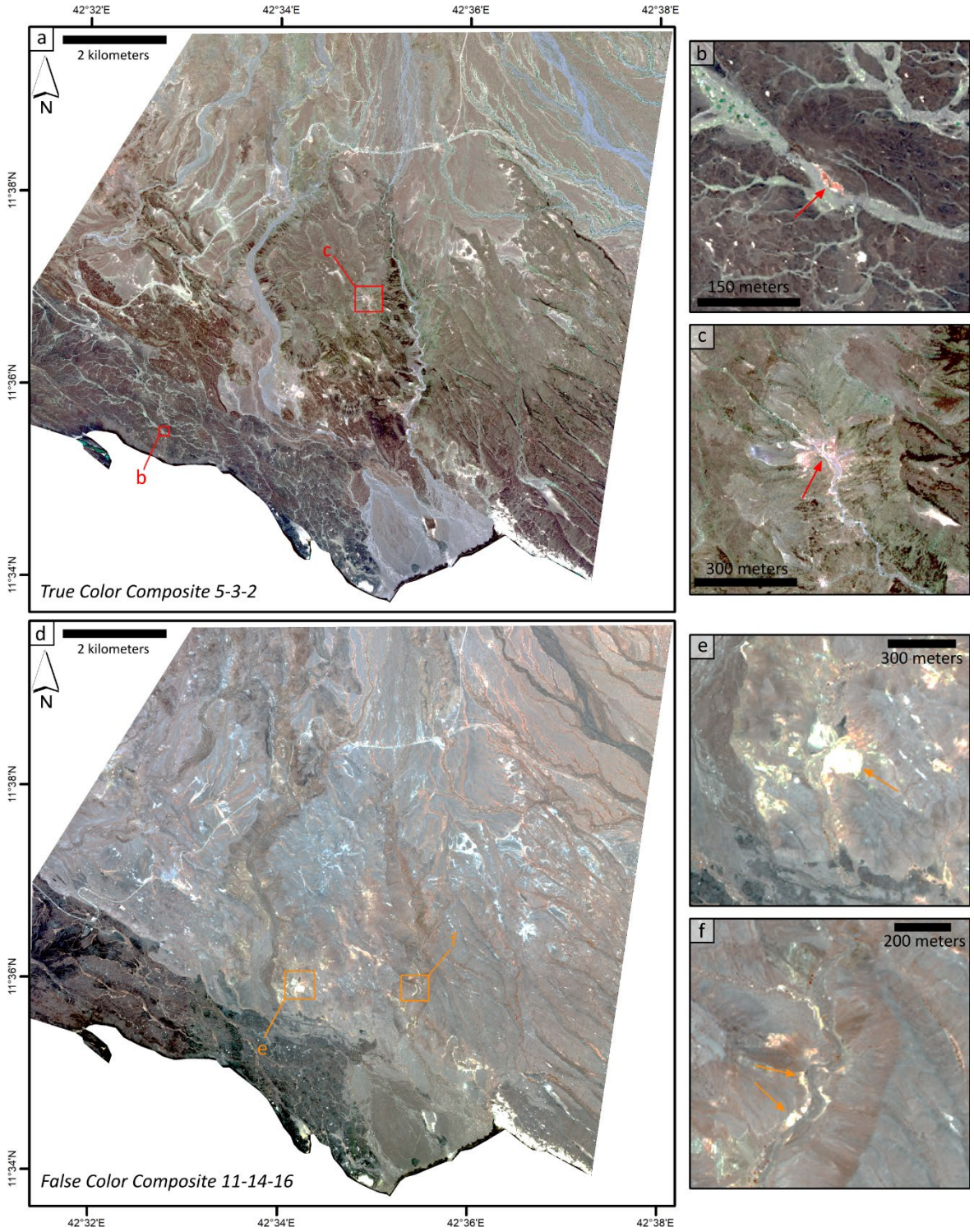


*Figure 5.5: (a) True color composite of the WV-3 scene, bands 5-3-2 (RGB). (b) and (c) show locations of altered material that is appearing in orange colors, as indicated by the red arrows. (d) False color composite of the WV-3 scene, SWIR band combination 11-14-16. (e) and (f) show alteration zones that appear in bright colors in this band combination, as indicated by the orange arrows. (e) shows an alteration zone with specifically great extent, while (f) shows alteration locations along the walls of Wadi Analé.*

Regarding the visualization of alteration zones by composite images, the true color composite of WV-3 VNIR bands 5-3-2 reveals useful information, as these bands span the $Fe^{3+}$ absorption feature (Figure 5.3c). The iron-rich areas are appearing in red to orange colors on Figure 5.5a, b & c and are indicated by red arrows. The band combination of SWIR bands 11-14-16 shown in Figure 5.5d, e & f enhances the locations of clay minerals and carbonate minerals as these bands are covering the according absorption features (Figure 5.3a & b). Clay and carbonate mineral sites are appearing in bright colors as indicated by the orange arrows in Figure 5.5e & f. For wavelength ranges of the above used WV-3 bands see Table 1.

### *5.4.2 Band Ratioing*

The method of band ratioing is common for feature extraction and widely used for lithological and mineral mapping (Kruse et al. 2015, Mars 2018, Sabins 1997). In this method, the values of one band are divided by the values of another band for each pixel, resulting in a ratio image. The advantage of band ratios is that topographic and illumination effects are reduced while differences in spectral characteristic are highlighted in the resulting data (Karimzadeh & Tangestani 2019, Kruse et al. 2015, Lillesand et al. 2008, Sabins 1997).

Appropriate band pairs for ratio calculation are selected based on the spectral characteristics of the relevant mineral groups as described in chapter 5.3. Band ratios for each mineral group are summarized in Table 2 and results are shown in Figure 5.6. Large sized images are attached in the appendix. Descriptions of the results concentrate on the central part of the study area.

*Table 2: Band ratios generated for the enhancement of different mineral groups*

| Mineral Group | Iron bearing minerals | Al-OH bearing minerals | Carbonates |
|---|---|---|---|
| Band Ratio | $\frac{\text{VNIR 5}}{\text{VNIR 2}}$ | $\frac{\text{SWIR 14}}{\text{SWIR 15}}$ | $\frac{\text{SWIR 13}}{\text{SWIR 16}}$ |

#### *5.4.2.1 Iron bearing minerals*

The iron bearing minerals goethite, hematite and limonite show characteristic absorption features in several bands of the VNIR range at wavelengths between 0.49 and 0.85 µm (chapter 5.3, Figure 5.3). The ratio of the visible bands $\frac{red}{blue}$ is a widely used ratio for highlighting iron bearing minerals or, respectively, iron-stained alteration, using several multispectral sensors, like Landsat, ASTER or WV-3 (Cudahy 2012, Gopinathan et al. 2020, Sekandari et al. 2020, Shirazi et al. 2018). Regarding the WV-3 bands, the ratio $\frac{red}{blue}$ corresponds to the band ratio of WV-3 VNIR band 5 (red, center wavelength 0.66 µm) and VNIR band 2 (blue, center wavelength 0.48 µm) (see Table 1). The resulting band ratio image is displayed as a colored image in Figure 5.6a. Red pixels have a high ratio value and enhance areas with

increased occurrences of iron bearing minerals. A slight increase of the values at the known fumarolic locations can be identified by comparison with the WV-3 true color composite in Figure 5.6d. An accumulation of high values appears in the southern area in between the two wadi systems. Additionally, the lithology or rather outcropping basement rock appears to affect the results and leads to high background values as well, as visible by high iron bearing mineral occurrences in the northwestern part of the area.

#### *5.4.2.2 Al-OH bearing minerals*

Absorption features of Al-OH bearing minerals range between 2.17 µm and 2.2 µm (chapter 5.3, Figure 5.3), covered by the SWIR bands 13, 14 and 15, while specifically the absorption in SWIR band 14 is characteristic for Al-OH bearing minerals (Mars 2018, Sun et al. 2017).

During the analysis, it was found that the SWIR bands 13, 14 and 15 in the present data set are strongly correlated, i.e. contain very similar information. In principle, band ratioing highlights the differences between the selected bands, and if the bands contain similar spectral information, the result is not carrying additional information. By taking the known fumarolic locations as reference points, the band ratio of bands SWIR 14 (center wavelength 2.205 µm) and SWIR 15 (center wavelength 2.260 µm) leads to the best results.

Figure 5.6b shows the band ratio of WV-3 bands 14/15. The occurrence of clay minerals based on this ratio correlates very well with the fumarolic sites as shown in Figure 5.6d. An area in the western catchment area of Wadi Afay shows an accumulation of increased occurrences of Al-OH bearing minerals, indicated by the white arrow.

#### *5.4.2.3 Carbonate minerals*

The spectral curves of carbonate minerals are characterized by the WV-3 SWIR bands 13 to 16, covering wavelengths of approximately 2.1-2.4 µm (Figure 5.3). Particularly SWIR band 16 defines the characteristic spectral absorption feature at wavelength of approximately 2.35 µm and is the characteristic band for information extraction by using band ratioing (Mars 2018, Salehi & Tangestani 2020, Sun et al. 2017). The ratio of SWIR band 13 and SWIR band 16 is used for enhancing the occurrence of carbonate minerals.

The resulting band ratio image is shown in Figure 5.6c and correlates very well with the known alteration locations shown in Figure 5.6d. The location in the western catchment area of Wadi Afay that already appeared in the Al-OH bearing ratio 14/15 (Figure 5.6b) is enhanced in this ratio as well (compare with white arrow, Figure 5.6b and c). A zone close to the coast in the southern part of the study area most probably represents evaporitic depositions rather than hydrothermally altered materials. This area is indicated by a black circle.

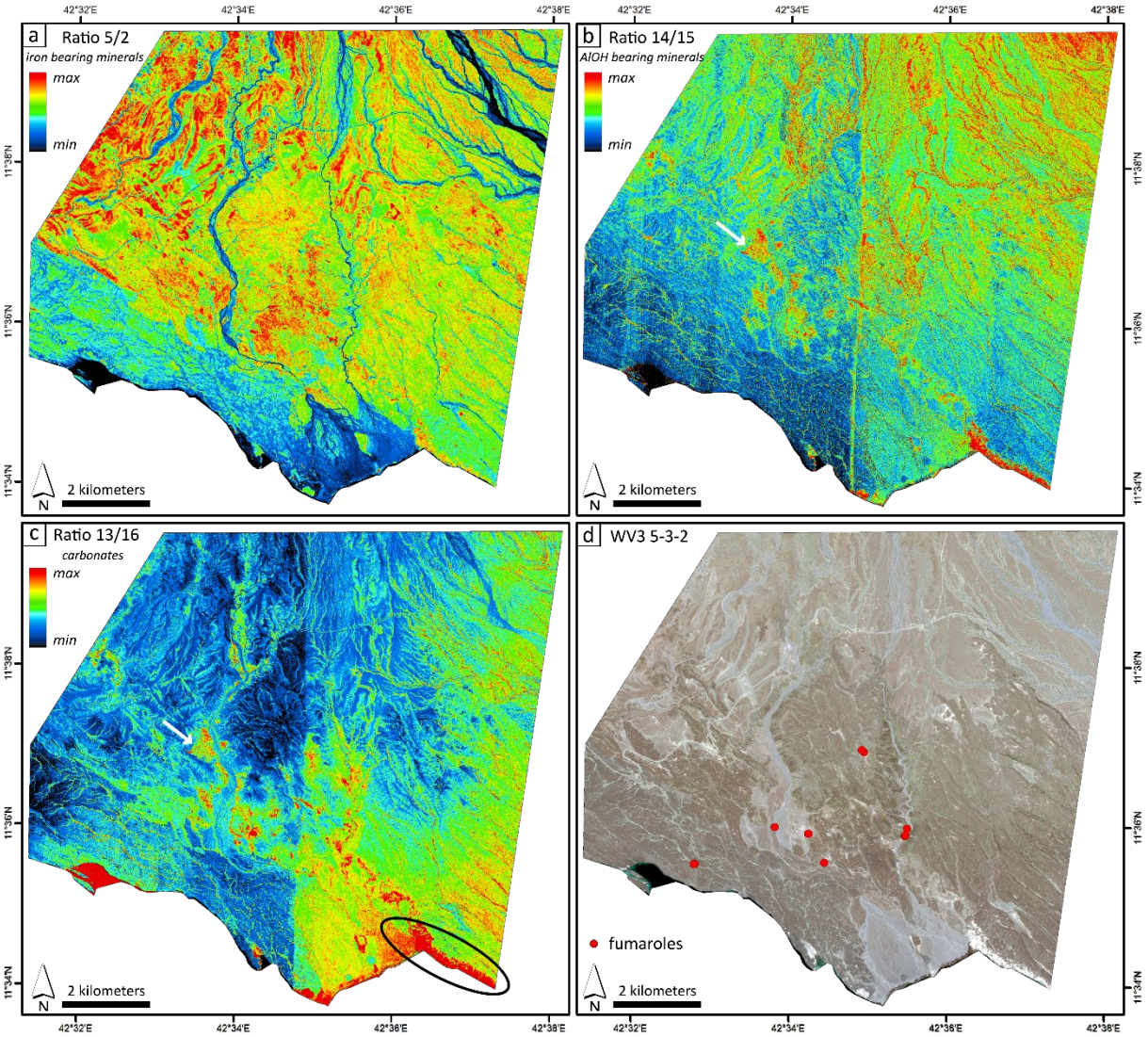


*Figure 5.6: Results for the chosen band ratio calculations for the enhancement of (a) iron bearing minerals (band ratio 5/2), (b) Al-OH bearing minerals (band ratio 14/15), and (c) carbonates (band ratio 13/16). The WV-3 band combination 5-3-2 is shown in (d) as well as the fumarole locations. By comparing the locations of fumaroles and the band ratio images in (a), (b) and (c), it can be seen that all mineral occurrences are enhanced in these sites. See the appendix for large-sized images.*

### *5.4.2.4 Band Ratioing: Summary*

The applied band ratios, as summarized in Table 2 and Figure 5.6, correlate well with the locations of known alteration sites, proving the method of band rationing as reliable for the identification of further alteration locations. The ratio images indicate yet unknown locations that might be of interest for further studies. For an accurate definition of these locations, the band ratios that were chosen for the representation of each mineral group are combined as a color composite as shown in Figure 5.7. The ratio 5/2 (iron bearing minerals) is assigned to the red channel, the ratio 14/15 (Al-OH bearing minerals) to the green channel and the ratio 15/16 (carbonates) to the blue channel. The resulting mixed colors and the corresponding composition of the three mineral groups are explained in the legend triangle (Figure 5.7a). In general, bright colors indicate the presence of all three mineral groups. Locations that appear

white in the composite image are locations with a balanced mixing ratio of all three mineral groups.

Generally, the color composite in Figure 5.7a as well as the generated band ratio image for iron bearing minerals (Figure 5.6a) both reveal that the content of iron bearing minerals is higher in the northwestern part of the study area. These increased contents are probably the result of topographic effects. At locations where the basement rock crops out due to higher elevation, it is not covered by fluvial/alluvial deposits and appears with a higher iron content than lower elevated areas, where a sediment cover exists.

The northeastern part of the study area majorly appears in combinations of blue and green colors in the band ratio combination (Figure 5.7) indicating an increased occurrence of Al-OH bearing minerals and carbonates. Depositions in this region are mainly caused by alluvial fans in a flat terrain, so that most probably alluvial deposits are responsible for a high Al-OH response and not hydrothermally altered materials. Near the coast in the southern part of the study area, blue colors indicate high carbonate mineral occurrences, most probably being the result of natural evaporation processes of seawater.

The occurrence of all three mineral groups overlap mainly in the central part of the study area, as indicated by bright colors in Figure 5.7a & b. Such locations can especially be identified in the area between the two major wadi systems and in the adjacent areas a few meters to the east and west and are outlined Figure 5.7b. Especially the circular shape of these locations attracts attention regarding their significance for the identification of hydrothermal activity. In some cases, fumarolic activity is already documented, which can be taken as evidence for the reliability of the results.

One location close to the western border of the WV-3 scene indicates the occurrence of all three mineral groups by its bright turquoise to bluish color, implying an increased proportion of Al-OH bearing minerals and carbonates compared to the iron bearing minerals. This location is marked in Figure 5.7a. The arrow points to a deflected stream representing a lineament intersection. The presence of a lineament intersection from a NNW-SSE striking structure that might facilitate fluid migration supports the suggestion that increased hydrothermal activity occurs at this location.

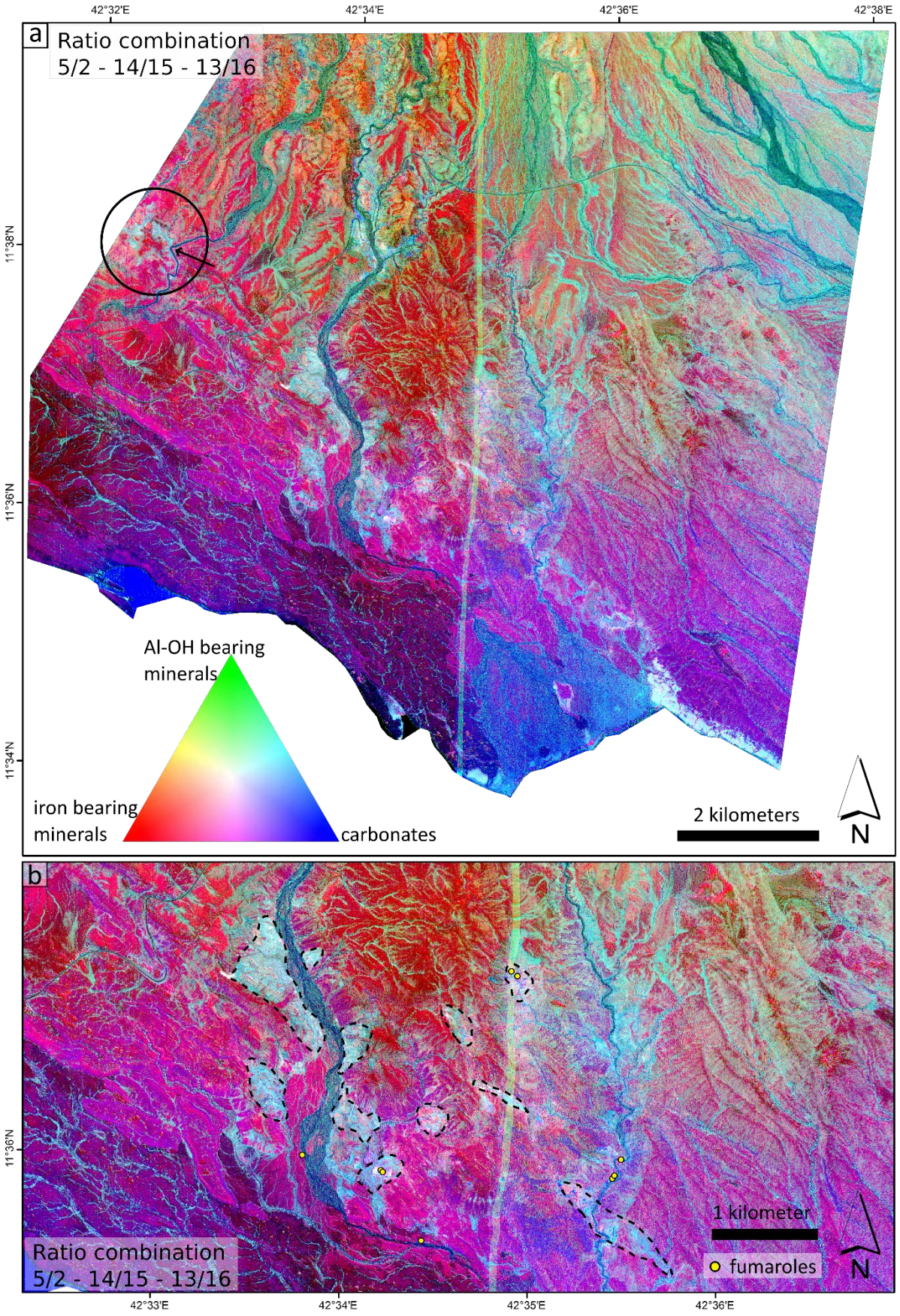


*Figure 5.7: (a) Color composite of the band ratios 5/2-14/15-13/16 (RGB). Iron bearing minerals are appearing in red, Al-OH bearing minerals in green and carbonates in blue colors. (b) additionally shows the locations of documented fumarolic sites. Areas where all three mineral groups occur are outlined in black.*

### *5.4.3 Classification Methods – SAM*

There are several classification methods to classify the image pixels based on their spectral information. During the process of classification, pixels are automatically labeled into classes. Classification methods can be either supervised or unsupervised. In a supervised classification, training areas are defined that are representative sample sites for a known cover type, or respectively, one class. The pixels of the satellite image are assigned to one class based on their similarity to the training classes. The unsupervised classification method classifies the pixels of an image without training data, grouping the pixels based on their spectral similarity. The identity of the resulting classes is unknown and is defined in a second step. (Gupta 2017, Lillesand et al. 2008)

***Spectral Angle Mapper- SAM***

For mapping minerals or mineral groups, there is a specific classification method called Spectral Angle Mapper (SAM), developed for analyzing hyperspectral data but also applicable for multispectral data with high spectral resolution such as WV-3 data. Spectral angle mapping is a supervised classification method analyzing the spectral reflectance curves (Gupta 2017, Kruse et al. 1993). The SAM determines the spectral similarity between the spectral reflectance curve of a reference mineral, e.g. from the USGS library, and the spectrum of the input data by calculating the angle between them (Elsaid et al. 2014, Kruse et al. 1993, van der Meer 2006). The angle is calculated for each pixel and is inversely related to the spectral similarity of the data, as a smaller angle represents higher correlation. By choosing the cosine of the angle as the SAM output, resulting values range between 0 and 1 with values closer to 1 representing a higher correlation, as it is presented in the following descriptions and figures.

The SAM was applied for several mineral groups. Minerals that were chosen for the SAM represent the mineral groups that are occurring in the study area and that were already investigated with band ratioing. The tool was executed on spectral reflectance curves that were resampled to the WV-3 spectral resolution (see Figure 5.3). The following interpretation of the results and the figures refer to the central part of the study area.

#### *5.4.3.1 Al-OH bearing minerals*

The clay minerals kaolinite, montmorillonite and muscovite are representative for the occurrence of Al-OH bearing minerals. Results of SAM for the individual minerals are shown in Figure 5.8. Since all three minerals have a very similar spectral profile, the result of the SAM is also very similar. Each of the results shows high correlation with the wadi streams and the drainage system, as clay minerals represent a significant amount of loose sediments that are transported by water runoff. Therefore, care has to be taken when interpreting these areas. Especially in the central part of the study area, several locations indicate an increased

occurrence of Al-OH bearing minerals, and most of these locations overlap in all of the three different SAM results. These sites are particularly noticeable because of their appearance as single spots rather than large areas. Some of the most extensive spots are indicated by black circles in Figure 5.8a to c and correlate with fumarolic sites that are already documented, as displayed for comparison in Figure 5.8d.

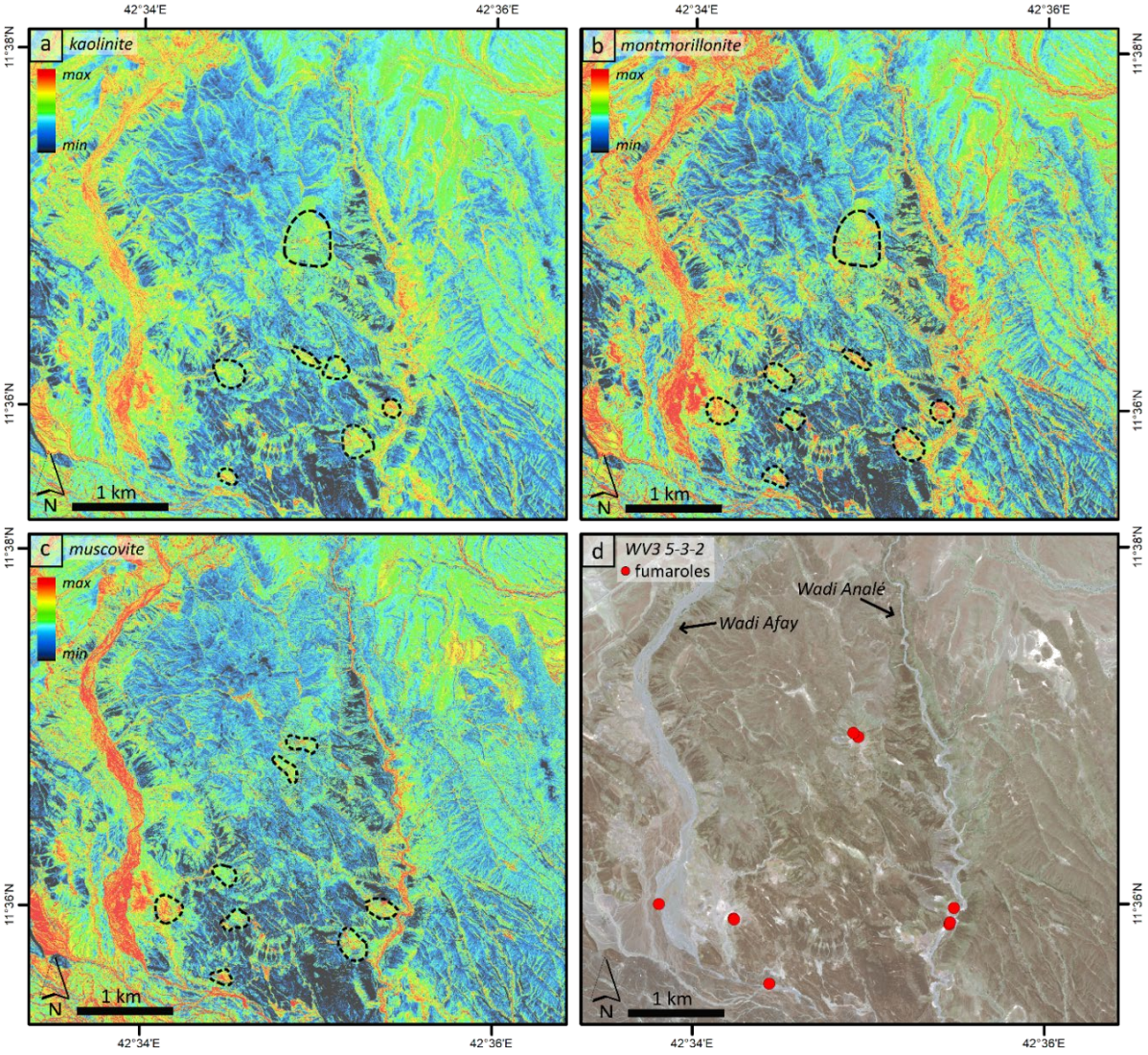


*Figure 5.8: SAM results for the Al-OH bearing minerals kaolinite (a), montmorillonite (b) and muscovite (c) in the central part of the study area. Red pixels indicate a high correlation with the respective minerals. Locations outlined in black indicate spots of particular interest due to high correlations and their circular shape. (d) True color composite of the WV-3 scene with the locations of documented fumaroles. All images show the same extent.*

### *5.4.3.2 Iron bearing minerals*

SAM results for the iron bearing minerals goethite, hematite and limonite are shown in Figure 5.9. Especially the results for goethite and hematite show a strong correlation with the youngest rift basalts in the southwestern part of the study area extent that is shown in Figure 5.9. Additionally, a circular area in the north shows high abundance of iron bearing minerals, also outlined in Figure 5.9a & b, which probably represents a young intrusion. In the geological map, this area is marked as External Rift Basalt while most of the study area consists of slightly

older Gulf Basalts. In the areas where Rift Basalts are present, a determination of specific locations of interest is not possible due to the high background correlation. The interpretation of the SAM results for these minerals has to be focused on the central/southern part of the study area, where a few locations should be considered for further interpretation and are marked in Figure 5.9. The result for limonite slightly differs from the goethite/hematite results and some locations with high correlation are appearing in the along Wadi Analé, especially to its western wall.

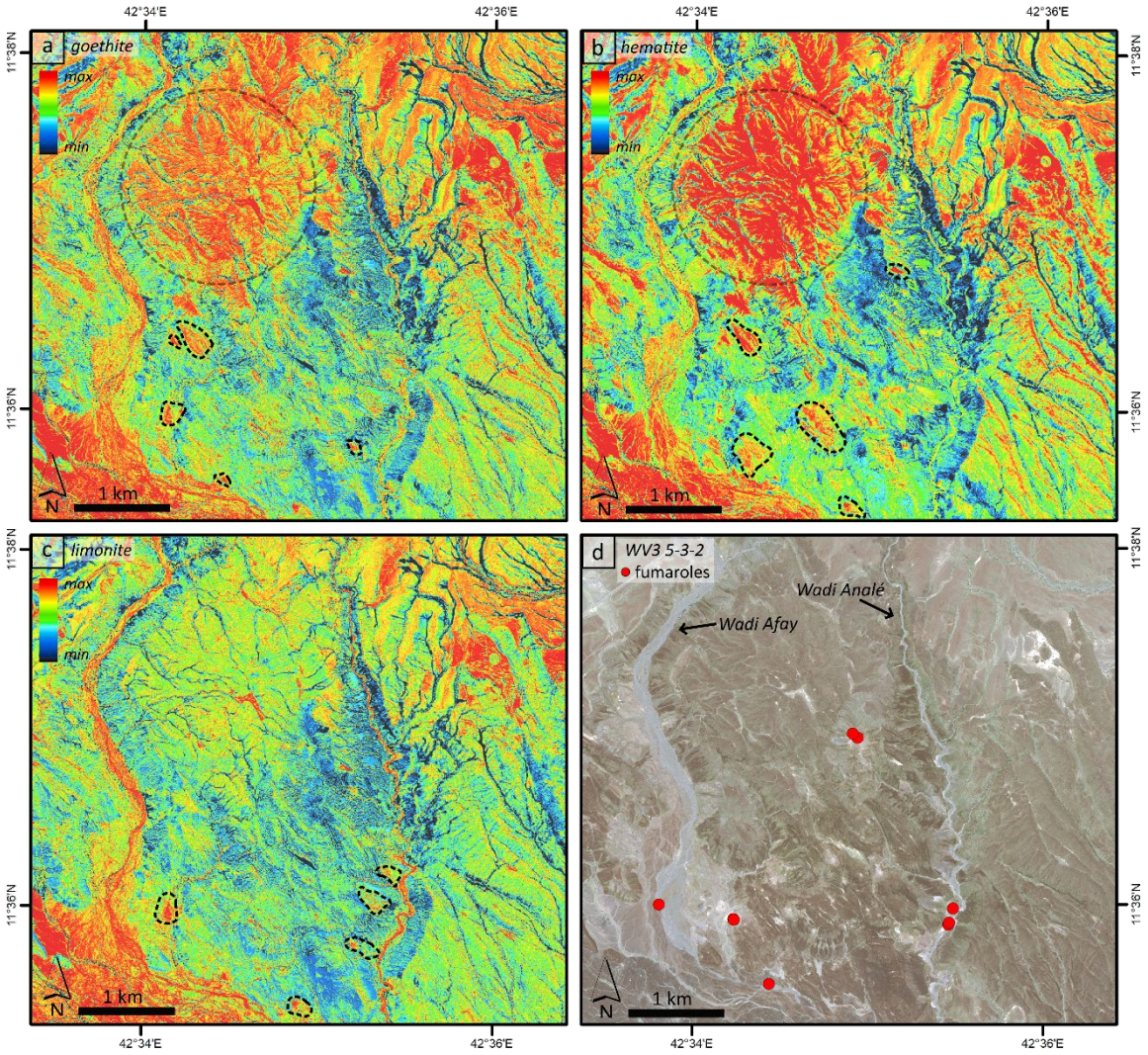


*Figure 5.9: SAM results for the iron bearing minerals goethite (a), hematite (b) and limonite (c) in the central part of the study area. Red pixels indicate a high correlation with the respective minerals. Locations outlined in black indicate spots of particular high correlations. A large circular area with increased values marked in (a) and (b) represents a young intrusion. (d) True color composite of the WV-3 scene with the locations of documented fumaroles. All images show the same extent.*

### *5.4.3.3 Carbonates*

The mineral calcite was chosen to be representative of the application of SAM to carbonate minerals because, due to the band width of WV-3, the results of calcite and dolomite are nearly identical (cf. Figure 5.3). The SAM result for calcite is displayed in Figure 5.10. Similar to the SAM results for Al-OH bearing minerals, the SAM result for calcite shows high correlation with

the wadi channels. West of Wadi Afay, the values show an increased correlation covering a quite extensive area, indicated in Figure 5.10. An accumulation of single spots with high correlation can be identified in the southeastern part of the extent. These single spots seem to be aligned in an area along a NW-SE oriented axis, this area is indicated by a black circle in Figure 5.10.

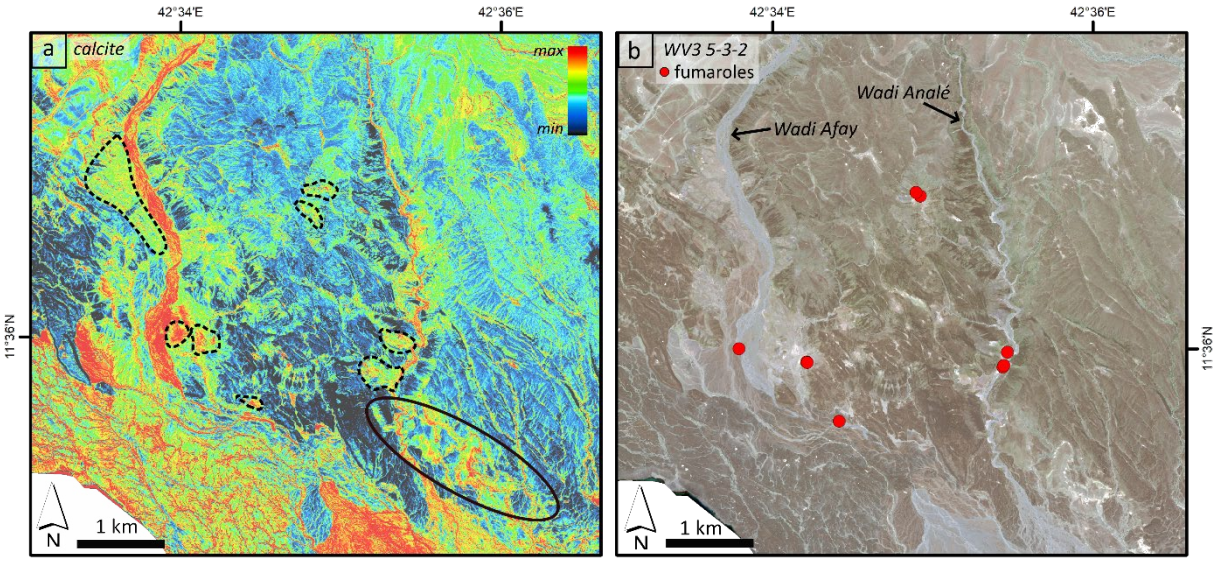


*Figure 5.10: (a) SAM result for calcite. Red pixels indicate a high correlation with the respective minerals. Locations outlined in black indicate spots of particular high correlations. Especially noticeable is an extensive area west of Wadi Afay and the NW-SE oriented longitudinal area where a high correlation indicates the occurrence of carbonate minerals. (b) True color composite of the WV-3 scene with the locations of documented fumaroles. Both images show the same extent.*

#### *5.4.3.4 SAM: Summary*

The results of SAM vary for each mineral group. The SAM results for the Al-OH bearing minerals kaolinite, montmorillonite and muscovite show high correlation with the drainage system, as these minerals often form a considerable amount of the sediment load transported and deposited by streams. The SAM results for iron bearing minerals are strongly related to the occurrence of young basalts. This is for example the case in the southwestern part of the area where the rift basalts are deposited, and a young External Rift Basalt intrusion in between Wadi Afay and Wadi Analé that appears as a circular structure in the above-mentioned results. These areas have to be interpreted with care while the focus of the SAM results will be set to areas with lower background response.

Especially in the central/southern part of the area in between Wadi Afay and Wadi Analé, numerous locations are highlighted in the results and overlap for several minerals, as it can be seen by comparing Figure 5.8 to Figure 5.10. A slight NW-SE trend is observable in these results through the alignment of mineral occurrences.

### *5.4.4 Principal Component Analysis – PCA*

The Principal Component Analysis (PCA) is a statistical method that is widely used for information extraction of different multispectral and hyperspectral data sets (Crosta et al. 2003, Elsaid et al. 2014, Farahbakhsh et al. 2016, Sun et al. 2017).

This method transforms the original spectral bands of a dataset into a set of principal component images. The number of principal components (PC) corresponds to the number of input bands, in this case 16. During the transformation process, the correlated original data is projected on new, uncorrelated axes, resulting in principal component images with less redundancy (Abubakar et al. 2019, Lillesand et al. 2008, Sun et al. 2017). The first principal components of multispectral data sets contain the most information (the information that occurs in most of the bands), and with increasing principal component number, the information content decreases. Topographic, structural, geological, and mineral information are concentrated in the first principal components, while noise is mainly visible in the higher principal component images (Elsaid et al. 2014, Farahbakhsh et al. 2016).

The statistical correlation of the new PC bands and the original input bands can be read in the eigenvector matrix. The eigenvectors are values indicating the proportion that each of the input bands contributes to the PC band. Hence, the eigenvectors derive essential information for the interpretation of PCA results. The so-called eigenvector loadings derive information about which spectral properties are responsible for the statistical variance mapped in each PC (Abhary & Hassani 2016). In other words: the eigenvector loadings enable the determination which PC contains the spectral information of the minerals of interest and whether they appear as high or low values (Crosta et al. 2003).

Each mineral or mineral group has indicative absorption features at specific wavelength ranges that can be used for mineral mapping, as described in chapter 5.3. Strong reflectance or a strong absorption in specific wavelength regions or bands is characteristic for each mineral group. The eigenvector matrix provides information if a strong reflective or absorptive band contributes to a specific PC image. A positive eigenvector loading in the matrix (=high positive values) in a reflective band enhances the minerals in bright colors, while a large negative loading in a reflective band enhances the minerals in dark colors referring to a grey scale image visualization.

Table 3 shows the eigenvector matrix derived from the PCA for all 16 WV-3 bands. Red values represent the maximum value, green values the minimum value for the single PCs. Values that are enhanced by bold digits are referred to in the text.

*Table 3: Eigenvector loadings for the single PC images. Minimum values are indicated in green, maximum values in red. Values referred to in the text are enhanced by bold digits.*

| | VNIR | | | | | | | | SWIR | | | | | | | |
|---|---|---|---|---|---|---|---|---|---|---|---|---|---|---|---|---|
| Eigenv. | B1 | B2 | B3 | B4 | B5 | B6 | B7 | B8 | B9 | B10 | B11 | B12 | B13 | B14 | B15 | B16 |
| PC 1 | 0.028 | 0.035 | 0.043 | 0.053 | 0.059 | 0.075 | 0.084 | 0.084 | 0.404 | 0.460 | 0.413 | 0.355 | 0.310 | 0.270 | 0.266 | 0.242 |
| PC 2 | 0.009 | 0.030 | 0.058 | 0.050 | 0.033 | 0.171 | 0.239 | 0.236 | 0.672 | -0.068 | 0.076 | 0.015 | -0.346 | -0.253 | -0.313 | -0.326 |
| PC 3 | 0.228 | 0.273 | 0.316 | 0.361 | 0.387 | 0.404 | 0.323 | 0.270 | -0.206 | -0.046 | -0.205 | -0.174 | 0.074 | 0.067 | 0.100 | 0.129 |
| PC 4 | -0.246 | -0.248 | -0.207 | -0.273 | **-0.331** | 0.085 | 0.484 | 0.527 | -0.118 | -0.214 | -0.060 | 0.060 | 0.059 | 0.077 | 0.095 | 0.216 |
| PC 5 | -0.008 | 0.000 | 0.008 | 0.026 | 0.041 | -0.011 | -0.212 | -0.151 | 0.485 | -0.454 | **-0.359** | **-0.005** | -0.032 | 0.081 | 0.149 | **0.574** |
| PC 6 | 0.069 | 0.017 | -0.036 | -0.104 | -0.154 | -0.127 | 0.152 | -0.076 | 0.278 | 0.092 | -0.079 | -0.732 | 0.214 | 0.277 | 0.300 | -0.273 |
| PC 7 | -0.047 | 0.025 | 0.061 | 0.085 | 0.072 | 0.044 | 0.045 | -0.127 | -0.010 | -0.629 | 0.219 | 0.299 | 0.190 | 0.422 | 0.098 | -0.452 |
| PC 8 | -0.217 | -0.189 | -0.090 | 0.040 | 0.117 | 0.137 | -0.229 | 0.175 | 0.111 | 0.237 | -0.643 | 0.220 | **0.377** | **0.082** | -0.100 | -0.319 |
| PC 9 | 0.537 | 0.421 | 0.172 | -0.201 | -0.373 | -0.250 | -0.150 | 0.317 | 0.025 | -0.080 | -0.146 | 0.213 | 0.185 | -0.142 | 0.059 | -0.096 |
| PC 10 | -0.103 | -0.123 | -0.047 | 0.059 | 0.181 | 0.076 | -0.497 | 0.449 | 0.018 | -0.217 | 0.388 | -0.303 | 0.329 | -0.288 | 0.008 | 0.031 |
| PC 11 | -0.018 | -0.039 | -0.004 | 0.000 | 0.050 | 0.024 | -0.352 | 0.342 | -0.053 | 0.102 | -0.043 | 0.046 | -0.635 | 0.290 | 0.479 | -0.145 |
| PC 12 | 0.066 | 0.081 | 0.051 | -0.041 | -0.130 | 0.055 | -0.204 | 0.173 | -0.025 | 0.057 | 0.071 | -0.160 | -0.068 | 0.623 | -0.661 | 0.172 |
| PC 13 | -0.105 | 0.037 | -0.008 | 0.065 | 0.484 | -0.797 | 0.193 | 0.238 | 0.023 | -0.012 | -0.047 | 0.022 | -0.011 | 0.081 | -0.096 | 0.034 |
| PC 14 | 0.636 | -0.254 | -0.685 | 0.057 | 0.213 | 0.068 | 0.049 | 0.001 | 0.001 | -0.037 | 0.002 | 0.032 | -0.012 | 0.053 | -0.036 | -0.006 |
| PC 15 | -0.005 | -0.169 | -0.040 | 0.838 | -0.470 | -0.204 | 0.004 | 0.068 | 0.002 | 0.005 | -0.007 | 0.002 | -0.002 | -0.012 | 0.005 | 0.010 |
| PC 16 | -0.337 | 0.728 | -0.579 | 0.119 | -0.027 | 0.073 | -0.020 | 0.012 | 0.001 | 0.004 | 0.001 | -0.012 | -0.004 | -0.010 | 0.018 | -0.003 |

As described in chapter 5.3, the investigated iron bearing minerals have characteristic absorption features in the VNIR bands (bands 1-8) (Figure 5.3), thus the eigenvector loadings of these bands are of specific interest. PC 4 shows a high negative loading from VNIR band 5 which is close to the iron absorption feature at approximately 0.7 µm. Iron bearing minerals are represented by low values in this PC image.

The carbonate minerals dolomite and calcite have a characteristic absorption feature in SWIR band 16. PC 5 has a high positive loading from SWIR band 16, and opposite signs from the reflective SWIR bands 10, 11 and 12. Carbonate minerals are represented by low values in this PC image, as the absorption band 16 has high positive loadings.

The Al-OH bearing minerals have a characteristic absorption feature in the SWIR bands 13, 14 and 15. The eigenvector matrix shows that the reflective band 13 has a high positive loading in the PC 8, with moderate to low loadings in absorption band 14. Al-OH bearing minerals are represented by high values in PC 8.

The single PC images representing the mineral groups are displayed as a colored image in Figure 5.11. The PC images 4 and 5 were inverted so that all images are displaying the mineral groups of interest with high values and in the same color, according to the chosen color ramp in red. All three images show different characteristics and diverse areas where the mineral groups accumulate. While PC 4 (Figure 5.11a) indicates an occurrence of iron bearing minerals especially along the wadi systems, PC 5 (Figure 5.11b) shows an increased occurrence of carbonate minerals in the south of the area towards the coast. PC 8 (Figure 5.11c) highlights especially the west of the study area with increased occurrences of Al-OH bearing minerals.

Despite these variations, some sites of increased mineral occurrences correlate on all three PC images. These are located in the southern area between the two wadi systems. To better

define these locations, an RGB composite was created from the individual PC images. This PC image combination from PC bands PC 4, PC 5 and PC 8 is shown in Figure 5.12.

The combination of these three images leads to the identification of locations where the increased occurrences of all three selected principal components overlap. Due to the color mixing, these sites will appear in bright colors in Figure 5.12. These are areas where alteration most likely occurs, outlined in Figure 5.12b. As with the results of the other methods used, increased occurrences are noted especially in the southern area in between the major wadi systems. One site at the western border of the study area indicates a correlation of all three mineral groups as well and is specified by the black circle in Figure 5.12a.

Compared to the band ratio color combination in Figure 5.7, the PCA results enhance similar locations in the area in between the wadi systems, and additionally enhance a few locations along Wadi Analé that are not as visible in the ratio result.

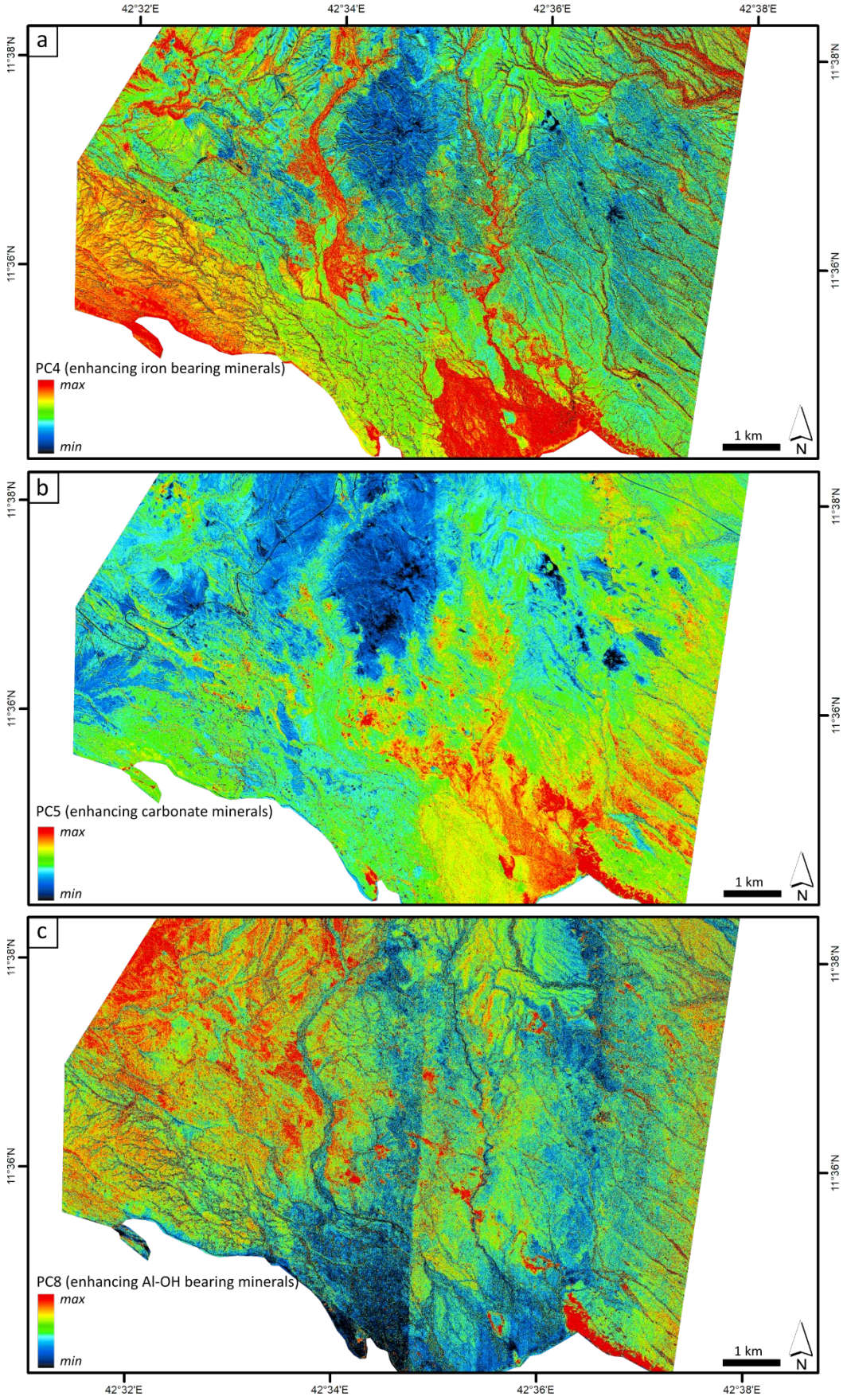


*Figure 5.11: Selected PC images enhancing the investigated minerals groups colored from black to red. Red colors represent high values. (a) PC4 for iron bearing minerals, (b) PC5 for carbonate minerals and (c) PC8 for Al-OH bearing minerals.*

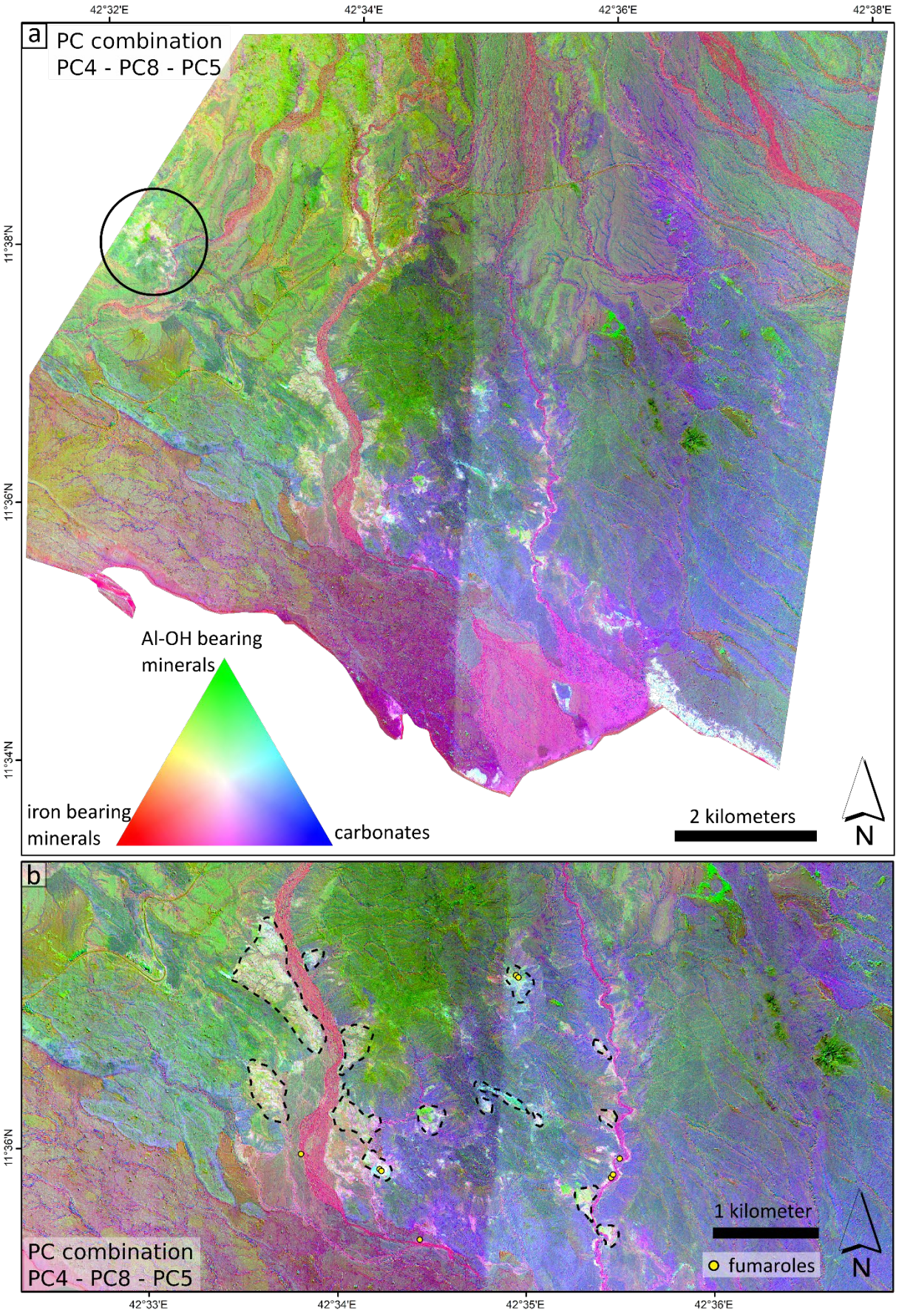


*Figure 5.12: PC combination PC4-PC8-PC5 (RGB). Where all mineral occurrences overlap, the locations will be colored white. The legend triangle represents the color mixings. Bright colors indicate the presence of all three mineral groups. These locations are outlined in (b).*

# 6 Results & Recommendation for further studies

***Mineral mapping***

The results of all three different methods provide comprehensive information on the distribution of hydrothermal mineral abundances throughout the study area of North Ghoubbet.

The northern part of the study area is significantly influenced by the run-off drainage systems from the Goda Mountains in the north and therefore unconsolidated sediments that were transported by the run-off dominate the depositions there. This leads to an increased occurrence of Al-OH bearing minerals in the band ratio, SAM and PCA results as clay minerals often form considerable amounts of the fluviatile transported particles. This complicates an appropriate interpretation of the results with respect to hydrothermal alteration zones in this area.

The occurrence of iron bearing minerals correlates strongly with the bedrock, as increased values correlate with young basalt formations close to the rift in the southeastern part of the study area and with a young intrusion between the wadi systems. Nevertheless, several locations are highlighted on the band ratio and SAM results corresponding with known hydrothermal alterations zones and documented fumaroles.

In addition to mapping techniques that identify minerals or mineral groups according to their spectral characteristics, a PCA was applied for a statistical analysis of the data.

Both approaches, spectral and statistical, enhance locations where the investigated mineral groups occur and where hydrothermal alteration most likely occurred and possibly still is active. Particularly, the band ratio color combination displayed in Figure 5.7 and the PC combination in Figure 5.12 enable a definition of alteration locations. In some cases, these results correlate with the locations of documented fumarolic and alteration sites, underscoring the validity and reliability of the results.

Locations where the different methods overlap are referred to as alteration sites in the following and are marked in Figure 6.1, showing the original WV-3 scene in a true color composite (bands 5-3-2) for the entire study area (Figure 6.1a) and specific extents (Figure 6.1b & c). Orange polygons mark areas where the mineral mapping results hint to increased occurrence of the investigated mineral assemblages. Areas where hydrothermal alteration is already documented and investigated in the field are mapped as well to evaluate if the mineral occurrences show any patterns. This map is also attached in the appendix.

As described throughout chapter 5.4, especially the southern part of the area that is bordered by the two wadi systems Wadi Afay and Wadi Analé attracts attention for further analysis and the locations where several of the investigated mineral assemblages occur are accumulating

there. This zone is marked as the center of hydrothermal activity in Figure 6.1b, indicated by the green ellipse.

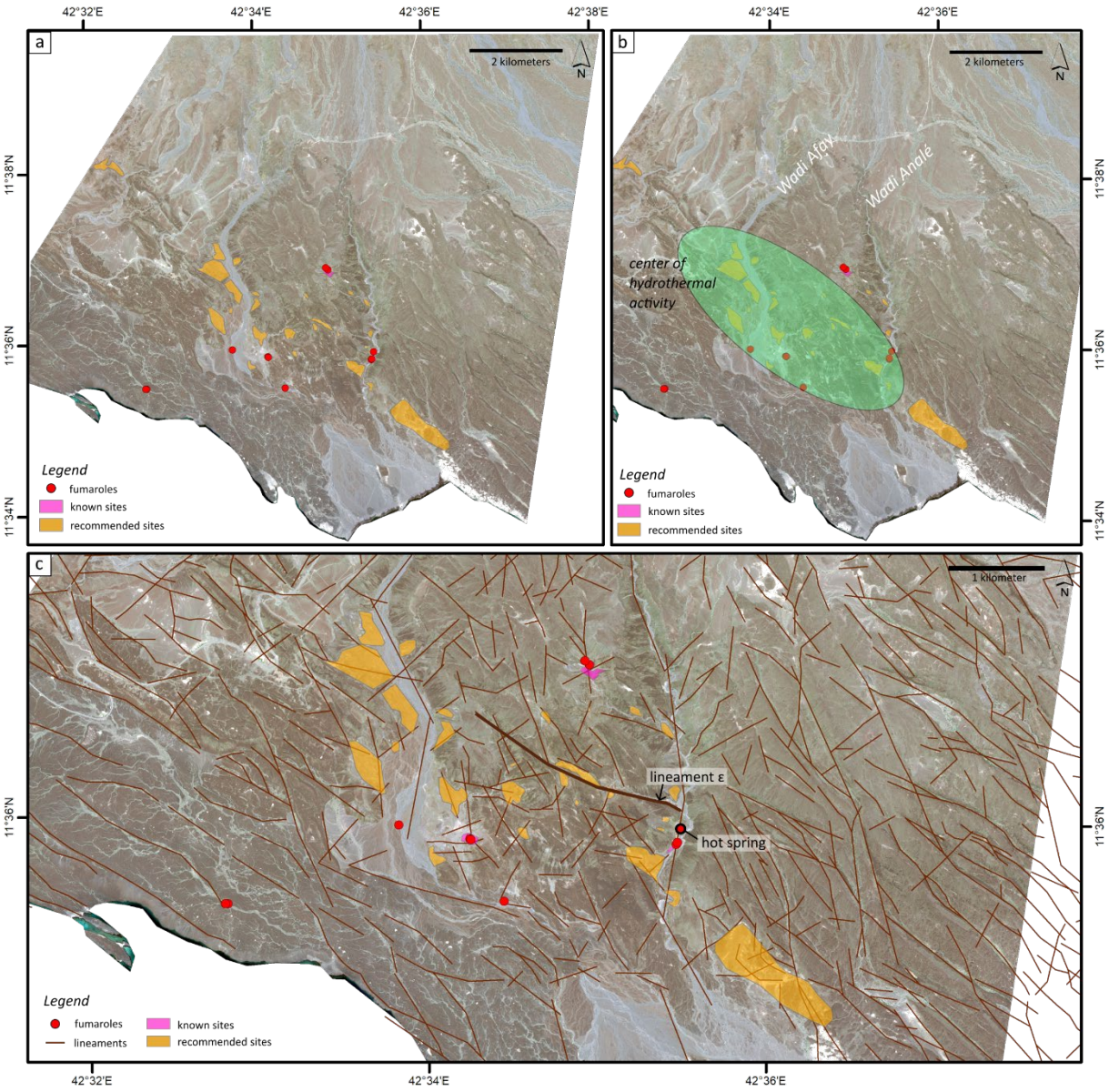


*Figure 6.1: True color composite of the WV-3 scene. The locations where mineral mapping techniques indicate alteration mineral assemblages are marked as orange polygons. The green zone in (b) shows the presumed center of hydrothermal activity. (c) shows the occurrence of hydrothermal alteration in combination with the lineaments that were detected in an earlier study.*

### *Linearity of mapping results and correlation with lineament map*

The green polygon in Figure 6.1b roughly covers the center of hydrothermal activity and extends along a NW-SE oriented longitudinal axis. This suggests that the increased hydrothermal activity is associated with a wide fault zone extending along this NW trending area, visible especially by the alignment of alteration zones.

Compared to the lineament map (Figure 6.1c), lineaments in this area appear in several directions with numerous intersections. This zone includes one major lineament (lineament ε), that was assessed as an essential structure facilitating fluid migration during lineament

analysis and is marked in Figure 6.1c. The occurrence of hydrothermal alteration minerals along this structure supports its assumed importance for the permeability in the area. The area where this structure meets Wadi Analé can be considered of particularly high geothermal potential, as proven by a hot spring location with temperatures well over 100°C, plotted in Figure 6.1c.

One area of interest is defined somewhat distant from the presumed center of hydrothermal activity between the wadi systems (Figure 6.1a). This site is located in the northwest of the study area close to the border of the WV-3 image, thus following the NW-orientation of the defined center of hydrothermal activity, or may even indicate an extension of this area towards the northwest. This location was already described in the context of band ratio results in chapter 5.4.2, as all ratio images indicate the occurrence of alteration minerals. PCA results indicate an accumulation of alteration minerals as well, as described in chapter 5.4.4. This area is recommended for field verification of the remote sensing results.

In summary, the analysis led to the identification of presumed alteration locations on a larger scale. The area that covers mostly all the recommended alteration sites can be interpreted as one large NW-oriented elliptic zone of approximately 3 kilometers width, most probably representing a wide fault zone. This zone also includes major lineaments and fumarolic sites, supporting the assessment of this zone as a zone of considerable geothermal potential. The individual locations where hydrothermal alteration minerals occur are recommended for field investigations.

# 7 Conclusion and Outlook

This study demonstrates that the mapping of mineral assemblages is a helpful tool for locating and estimating hydrothermal activity within the exploration phase of a potential geothermal site. WV-3 data form a very good basis for the detection of mineral occurrences with high spatial and spectral resolution. The combination of different information extraction techniques like band ratioing, spectral angle mapping and principal component analysis applied on the high-resolution data set enables the mapping of mineral assemblages.

In case of the North Ghoubbet working area, studies conducted up to this point, including lineament and alteration mapping and the locations of fumaroles known from the field, indicate an appreciable potential in the same area. This area is located in the south of North Ghoubbet and can be described by a NW oriented ellipse. Especially the overlapping areas with the wadi systems prove fluid migration by fumaroles and increased occurrences of hydrothermal alteration minerals.

A good supplement to this study would be the investigation of altered material in a laboratory with exact mineral analysis. Laboratory results can then be combined with remote sensing data, contributing to an improved specification including endmember specification and approving the mapping of the hydrothermal alteration mineral occurrences. The mineral distribution throughout an area might also act as an indicator for the location of the heat source. For example, Markússon & Stefánsson (2011) studied the geothermal surface alteration distribution in basalts of the Iceland geothermal reservoir. They observed that an assemblage of the iron oxides/hydroxides hematite and goethite along with montmorillonite are typical for medium to low activity areas in the flanks of the geothermal system. Regarding the entire Asal-Ghoubbet rift system as one large geothermal system, this categorization might suit as well. Although it should be noted that the composition of hydrothermal fluids might be different in Iceland and Djibouti, which has a significant influence in the chemistry of alteration processes.

Regarding further studies for the exploration of geothermal sites, several approaches would contribute to a better understanding of the geothermal reservoir in North Ghoubbet. A field verification of the mapped alteration zones is recommended for an assessment of the mineral mapping results. In addition to that, mineralogical investigations of altered material in the laboratory lead to a refinement of the results derived by satellite data.

Particularly the investigation of land surface temperature by applying either spaceborne or airborne data, collected for example by drones, is a good addition to the previously implemented methods. Combining information about land surface temperature with the lineament mapping and alteration mapping results would significantly contribute to an understanding of the geothermal system as a whole.

# 8 References

Abhary, A., & Hassani, H. (2016). Mapping hydrothermal mineral deposits using PCA and BR methods in Baft 1: 100000 Geological sheet, Iran. *International Journal of Advanced Engineering, Management and Science*, *2*(9), 239620.

Abubakar, A. J. A., Hashim, M., & Pour, A. B. (2019). Identification of hydrothermal alteration minerals associated with geothermal system using ASTER and Hyperion satellite data: a case study from Yankari Park, NE Nigeria. *Geocarto International*, *34*(6), 597-625.

Aden, M., Koichiro, W., Thomas, T. (2018). Sub-surface geology of hydrothermal alteration and 3D geological model of the wells GLC-1, ASAL 3, 4, and 5 in Asal-Rift geothermal field, Djibouti. Proceedings of 7th African Rift geothermal Conference.

Berger B.R. (1998). Hydrothermal alteration. *In*: Geochemistry. Encyclopedia of Earth Science. Springer, Dordrecht. https://doi.org/10.1007/1-4020-4496-8_162

Beyene, A., & Abdelsalam, M. G. (2005). Tectonics of the Afar Depression: A review and synthesis. *Journal of African Earth Sciences*, *41*(1-2), 41-59.

Brown, A. J., Walter, M. R., & Cudahy, T. J. (2005). Hyperspectral imaging spectroscopy of a Mars analogue environment at the North Pole Dome, Pilbara Craton, Western Australia. *Australian Journal of Earth Sciences*, *52*(3), 353-364.

Browne, P. R. L. (1978). Hydrothermal alteration in active geothermal fields. *Annual review of earth and planetary sciences*, *6*, 229-250.

Calvin, W. M., Littlefield, E. F., & Kratt, C. (2015). Remote sensing of geothermal-related minerals for resource exploration in Nevada. *Geothermics*, *53*, 517-526.

Chorowicz, J. (2005). The east African rift system. *Journal of African Earth Sciences*, *43*(1-3), 379-410.

Crosta, A. P., De Souza Filho, C. R., Azevedo, F., & Brodie, C. (2003). Targeting key alteration minerals in epithermal deposits in Patagonia, Argentina, using ASTER imagery and principal component analysis. *International Journal of Remote Sensing*, *24*(21), 4233-4240.

Cudahy, T. J. (2012). Australian ASTER Geoscience Product Notes,(Version 1), 7th August, 2012–CSIR0, ePublish No. EP-30-07-12-44.

De Chabalier, J. B., & Avouac, J. P. (1994). Kinematics of the Asal Rift (Djibouti) determined from the deformation of Fieale Volcano. *Science*, *265*(5179), 1677-1681.

DigitalGlobe, Inc. (2014). DigitalGlobe Imagery Support Data (ISD) Documentation, v.1.1.2. Available online: DigitalGlobe ISD Documentation.

Elsaid, M., Aboelkhair, H., Dardier, A., Hermas, E., & Minoru, U. (2014). Processing of multispectral ASTER data for mapping alteration minerals zones: as an aid for uranium exploration in Elmissikat-Eleridiya granites, Central Eastern Desert, Egypt. *The Open Geology Journal*, *8*(1).

Ermertz, A. 2020. Regional Project Geothermal Energy in East Africa: Lineament Analysis in North Ghoubbet (Tadjoura, Djibouti). Office Djiboutien de Développement de l'Énergie Géothermique (ODDEG) & Federal Institute for Geosciences and Natural Resources (BGR), Hannover.

Farahbakhsh, E., Shirmard, H., Bahroudi, A., & Eslamkish, T. (2016). Fusing ASTER and QuickBird-2 satellite data for detailed investigation of porphyry copper deposits using PCA; Case Study of Naysian Deposit, Iran. *Journal of the Indian Society of Remote Sensing*, *44*(4), 525-537.

Gopinathan, P., Parthiban, S., Magendran, T., Al-Quraishi, A. M. F., Singh, A. K., & Singh, P. K. (2020). Mapping of ferric (Fe3+) and ferrous (Fe2+) iron oxides distribution using band ratio techniques with ASTER data and geochemistry of Kanjamalai and Godumalai, Tamil Nadu, south India. *Remote Sensing Applications: Society and Environment*, *18*, 100306.

Gupta, R. P. (2017). Remote sensing geology – 2nd ed. Springer.

Houssein, D. E., & Axelsson, G. (2010). Geothermal resources in the Asal Region, Republic of Djibouti: An update with emphasis on reservoir engineering studies. *Geothermics*, *39*(3), 220-227.

Karimzadeh, Z., & Tangestani, M. H. (2019). Application of WORLDVIEW-3 Data in Alteration Mineral Mapping in Chadormalu Area, Central Iran. *The International Archives of Photogrammetry, Remote Sensing and Spatial Information Sciences*, *42*, 589-596.

Kokaly, R. F., Clark, R. N., Swayze, G. A., Livo, K. E., Hoefen, T. M., Pearson, N. C., Wise, R., A., Benzel, W. M., Lowers, H. A., Driscoll, R. L., & Klein, A. J. (2017). *USGS spectral library version 7* (No. 1035). US Geological Survey.

Kratt, C., Calvin, W. M., & Coolbaugh, M. F. (2010). Mineral mapping in the Pyramid Lake basin: Hydrothermal alteration, chemical precipitates and geothermal energy potential. *Remote Sensing of Environment*, *114*(10), 2297-2304.

Kruse, F. A., Lefkoff, A. B., Boardman, J. W., Heidebrecht, K. B., Shapiro, A. T., Barloon, P. J., & Goetz, A. F. H. (1993). The spectral image processing system (SIPS)-interactive visualization and analysis of imaging spectrometer data. In *AIP Conference Proceedings* (Vol. 283, No. 1, pp. 192-201). American Institute of Physics.

Kruse, F. A., Baugh, W. M., & Perry, S. L. (2015). Validation of DigitalGlobe WorldView-3 Earth imaging satellite shortwave infrared bands for mineral mapping. *Journal of Applied Remote Sensing*, *9*(1), 096044.

Le Gall, B., Daoud, M. A., Rolet, J., & Egueh, N. M. (2011). Large-scale flexuring and antithetic extensional faulting along a nascent plate boundary in the SE Afar rift. *Terra Nova*, *23*(6), 416-420.

Lillesand, T., Kiefer, R. W., & Chipman, J. (2008). *Remote sensing and image interpretation – 6th ed*. John Wiley & Sons.

Markússon, S. H., & Stefánsson, A. (2011). Geothermal surface alteration of basalts, Krýsuvík Iceland—Alteration mineralogy, water chemistry and the effects of acid supply on the alteration process. *Journal of Volcanology and Geothermal Research*, *206*(1-2), 46-59.

Mathieu, L. (2018). Quantifying hydrothermal alteration: A review of methods. *Geosciences*, *8*(7), 245.

Mas, A., Guisseau, D., Mas, P. P., Beaufort, D., Genter, A., Sanjuan, B., & Girard, J. P. (2006). Clay minerals related to the hydrothermal activity of the Bouillante geothermal field (Guadeloupe). *Journal of Volcanology and Geothermal research*, *158*(3-4), 380-400.

Mars, J. C. (2018). Mineral and lithologic mapping capability of WorldView 3 data at Mountain Pass, California, using true-and false-color composite images, band ratios, and logical operator algorithms. *Economic Geology*, *113*(7), 1587-1601.

Polun, S. G., Gomez, F., & Tesfaye, S. (2018). Scaling properties of normal faults in the central Afar, Ethiopia and Djibouti: Implications for strain partitioning during the final stages of continental breakup. *Journal of Structural Geology*, *115*, 178-189.

Sabins Jr, F. F. (1997). *Remote sensing-principles and interpretation*. W.H. Freeman and company.

Salehi, T., & H Tangestani, M. (2020). Evaluation of WorldView-3 VNIR and SWIR Data for Hydrothermal Alteration Mapping for Mineral Exploration: Case Study from Northeastern Isfahan, Iran. *Natural Resources Research*, *29*, 3479-3503.

Sekandari, M., Masoumi, I., Beiranvand Pour, A., M Muslim, A., Rahmani, O., Hashim, M., Zoheir, B., Pradhan, B., Misra, A., & Aminpour, S. M. (2020). Application of Landsat-8, Sentinel-2, ASTER and WorldView-3 spectral imagery for exploration of carbonate-hosted Pb-Zn deposits in the Central Iranian Terrane (CIT). *Remote Sensing*, *12*(8), 1239.

Shirazi, A., Hezarkhani, A., & Shirazy, A. (2018). Remote sensing studies for mapping of iron oxide regions, South of Kerman, Iran. *International Journal of Science and Engineering Applications*, *7*(4), 45-51.

Sun, Y., Tian, S., & Di, B. (2017). Extracting mineral alteration information using WorldView-3 data. *Geoscience Frontiers*, *8*(5), 1051-1062.

Teklemariam, M., Battaglia, S., Gianelli, G., & Ruggieri, G. (1996). Hydrothermal alteration in the Aluto-Langano geothermal field, Ethiopia. *Geothermics*, *25*(6), 679-702.

Van der Meer, F. (2006). The effectiveness of spectral similarity measures for the analysis of hyperspectral imagery. *International journal of applied earth observation and geoinformation*, *8*(1), 3-17.

Varet, J. (2010). Contribution to favorable geothermal site selection in the Afar triangle. In *Argeo Meeting, Djibouti, 17p*.

Vellutini, P. (1990). The Manda—Inakir rift, republic of Djibouti: A comparison with the Asal rift and its geodynamic interpretation. *Tectonophysics*, *172*(1-2), 141-153.

Zan, L., Gianelli, G., Passerini, P., Troisi, C., & Haga, A. O. (1990). Geothermal exploration in the Republic of Djibouti: thermal and geological data of the Hanlé and Asal areas. *Geothermics*, *19*(6), 561-582.

# 9 Appendix

## 9.1 Ratio maps entire scene

### *9.1.1 Iron bearing minerals, band ratio 5/2*

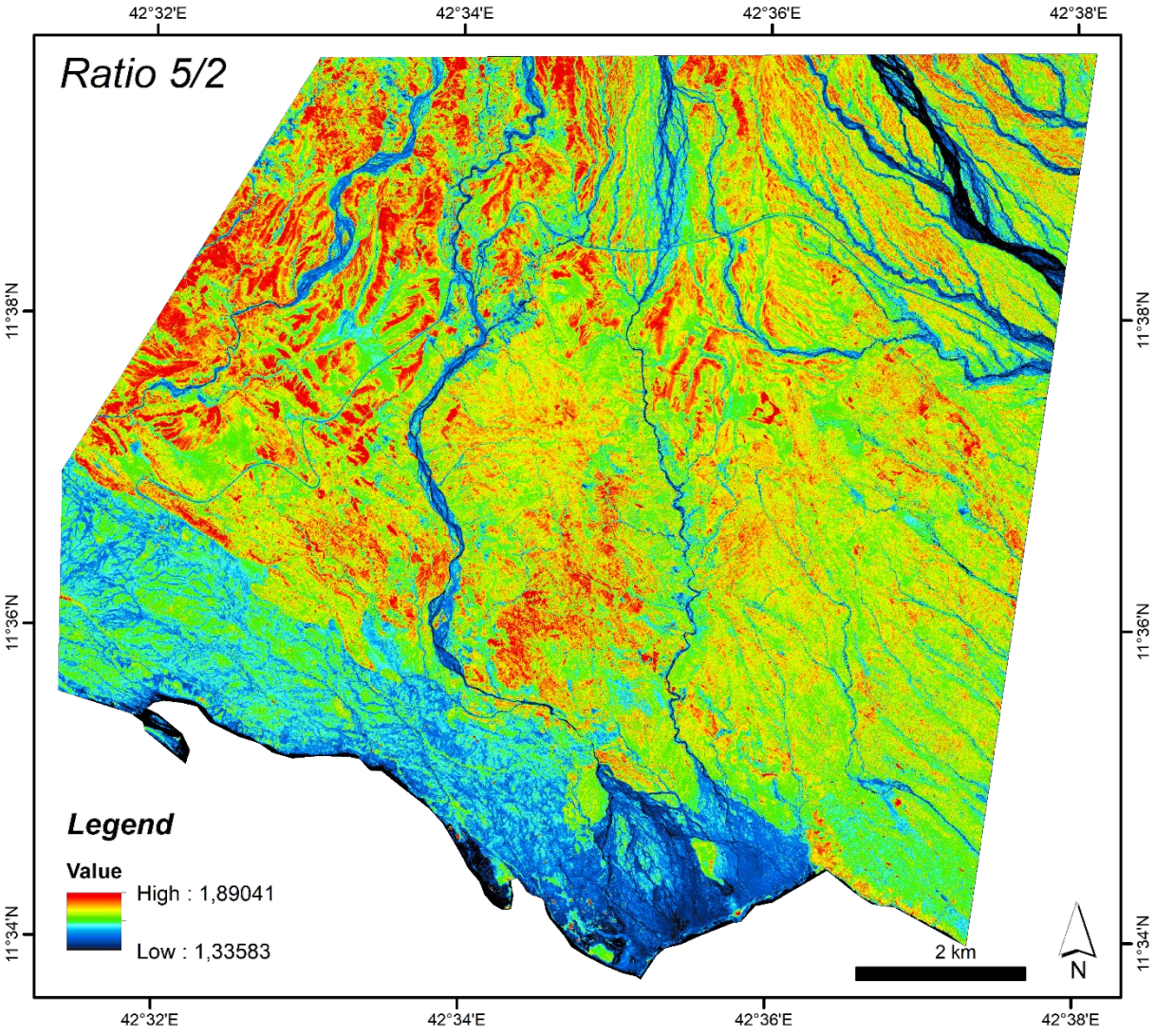

### *9.1.2 Al-OH bearing minerals, band ratio 14/15*

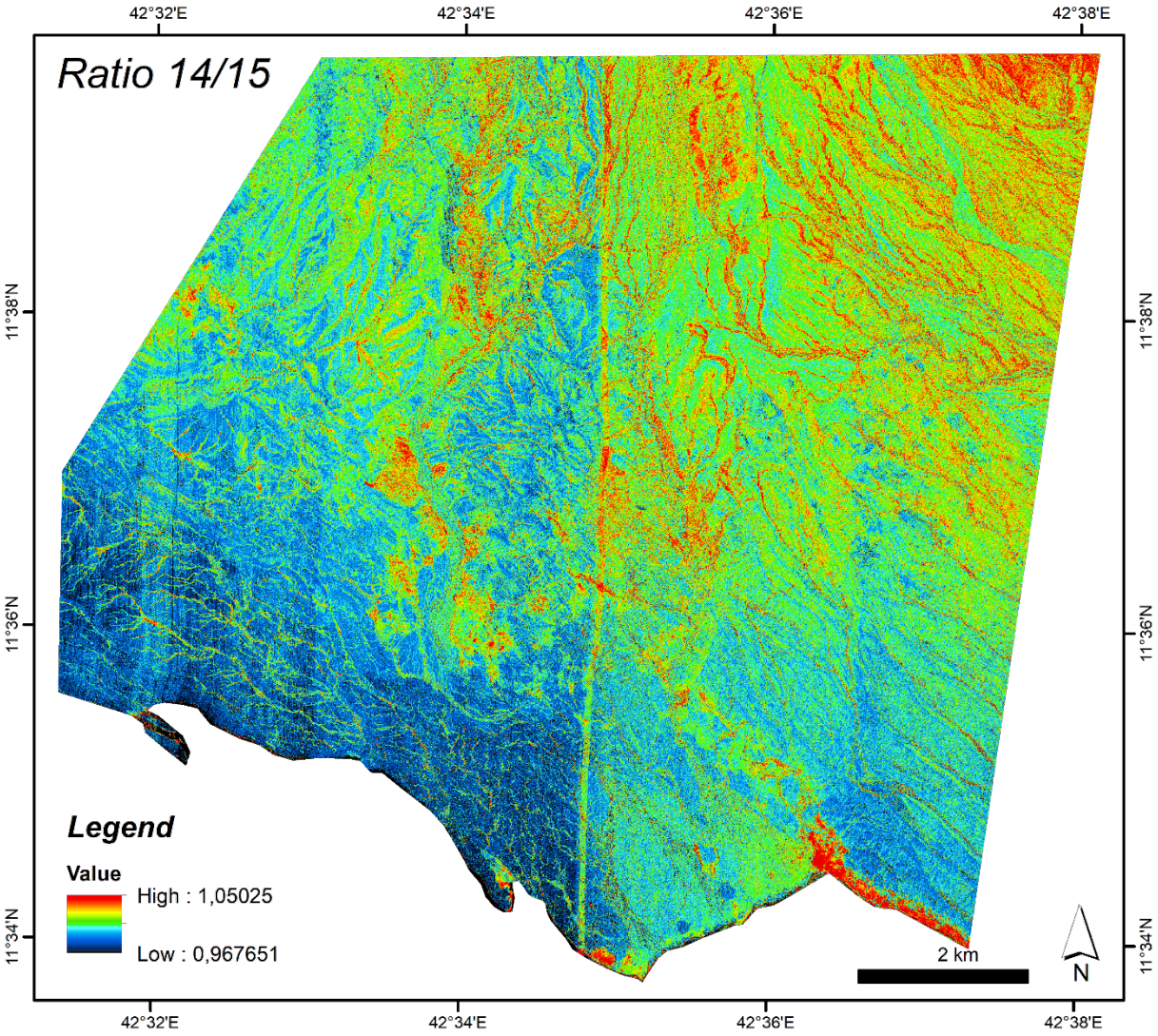

### *9.1.3 Carbonate minerals, bands 13/16*

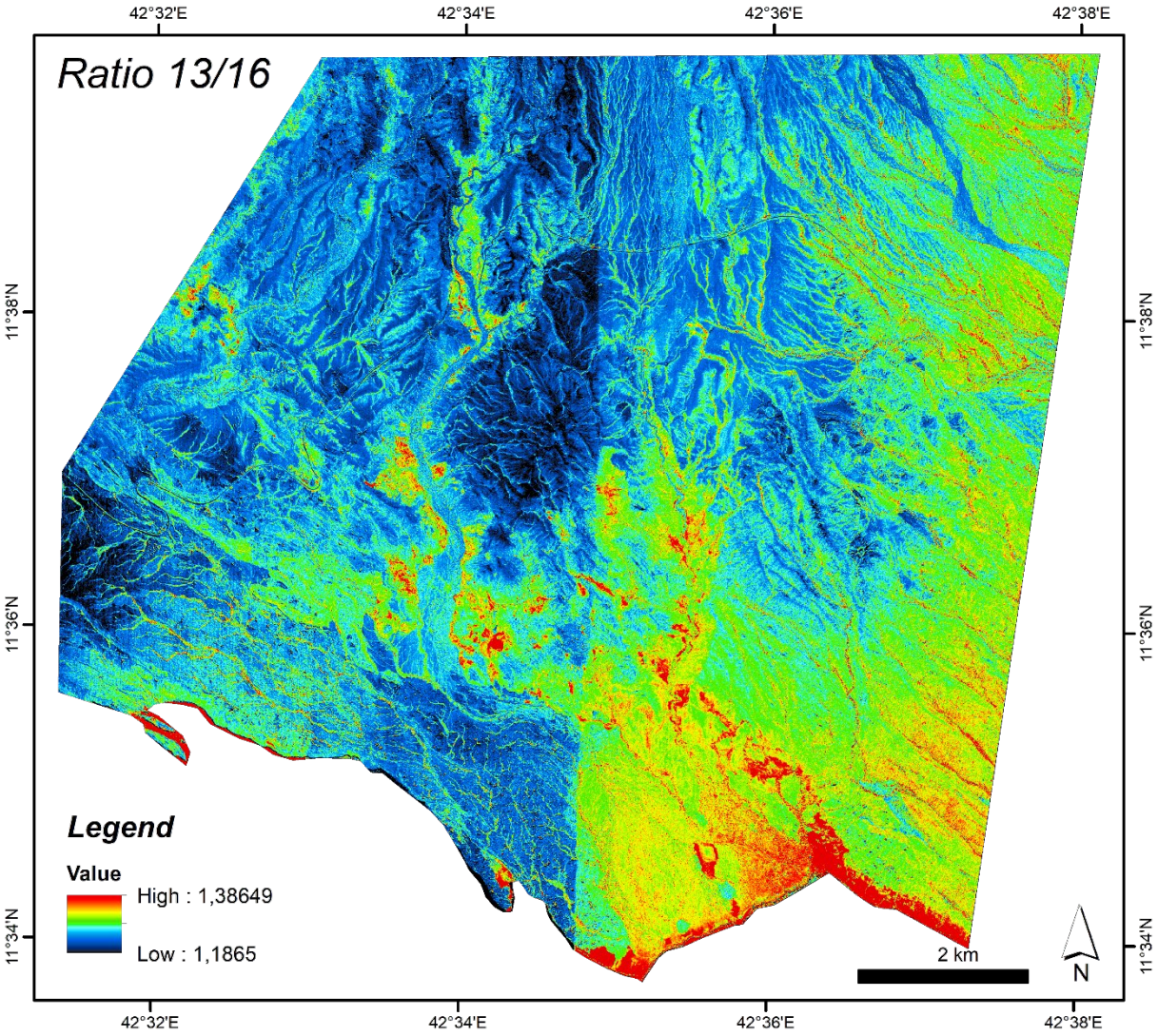

## 9.2 Presumed alteration zones entire scene

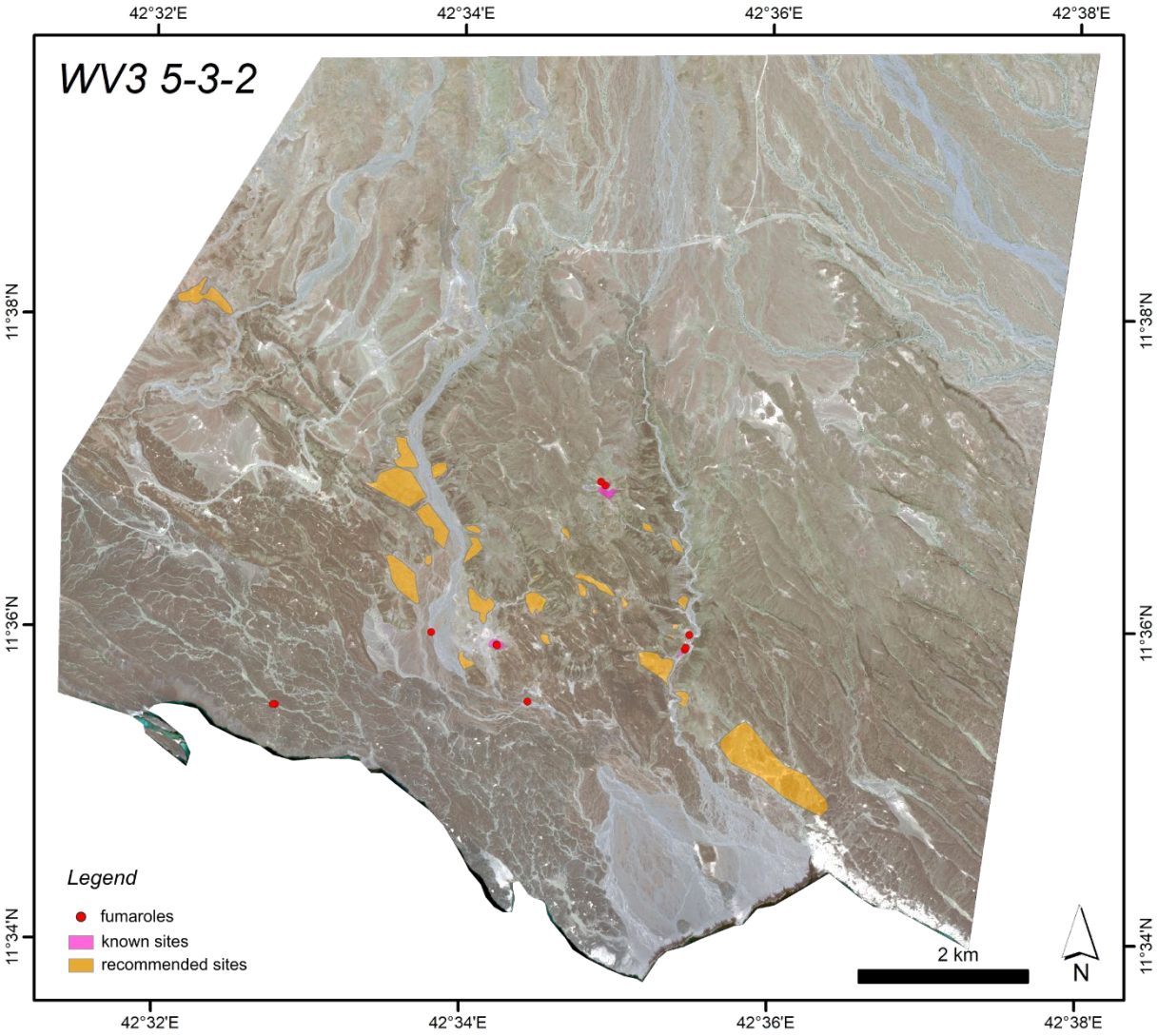

## 9.3 Field Evidence - Waypoints and Map

Waypoints (WPs) of measurements and field photos as mentioned in figures. The datum of the coordinates (Decimal degrees and UTM zone 16N) is WGS84.

| WP | Latitude | Longitude | Type | Temperature [°C] | Date |
|---|---|---|---|---|---|
| 01 | 42.573977 | 11.592250 | fumarole | 98.9 | 10.02.2020 |
| 02 | 42.570544 | 11.598300 | fumarole | 98 | 10.02.2020 |
| 03 | 42.570615 | 11.598229 | fumarole | 93 | 10.02.2020 |
| 04 | 42.563473 | 11.599594 | fumarole | 98.9 | 10.02.2020 |
| 05 | 42.546846 | 11.591433 | alteration | | 10.02.2020 |
| 06 | 42.546636 | 11.591756 | fumarole | 82.2 | 10.02.2020 |
| 07 | 42.546386 | 11.591766 | fumarole | 92.7 | 10.02.2020 |
| 08 | 42.546288 | 11.591968 | alteration | | 10.02.2020 |
| 09 | 42.582217 | 11.615384 | fumarole | 97 | 11.02.2020 |
| 10 | 42.581754 | 11.615767 | fumarole | 94.8 | 11.02.2020 |
| 11 | 42.582421 | 11.613914 | alteration | | 11.02.2020 |
| 12 | 42.586852 | 11.610445 | alteration | | 11.02.2020 |
| 13 | 42.589720 | 11.613063 | alteration | | 12.02.2020 |
| 14 | 42.589268 | 11.590554 | alteration | | 12.02.2020 |
| 15 | 42.590250 | 11.592366 | fault | | 12.02.2020 |
| 16 | 42.590094 | 11.596734 | alteration | | 12.02.2020 |
| 17 | 42.590965 | 11.597921 | fumarole | 98.2 | 12.02.2020 |
| 18 | 42.591071 | 11.598126 | fumarole | 98.7 | 12.02.2020 |
| 19 | 42.591425 | 11.599485 | fumarole | 108.5 | 12.02.2020 |

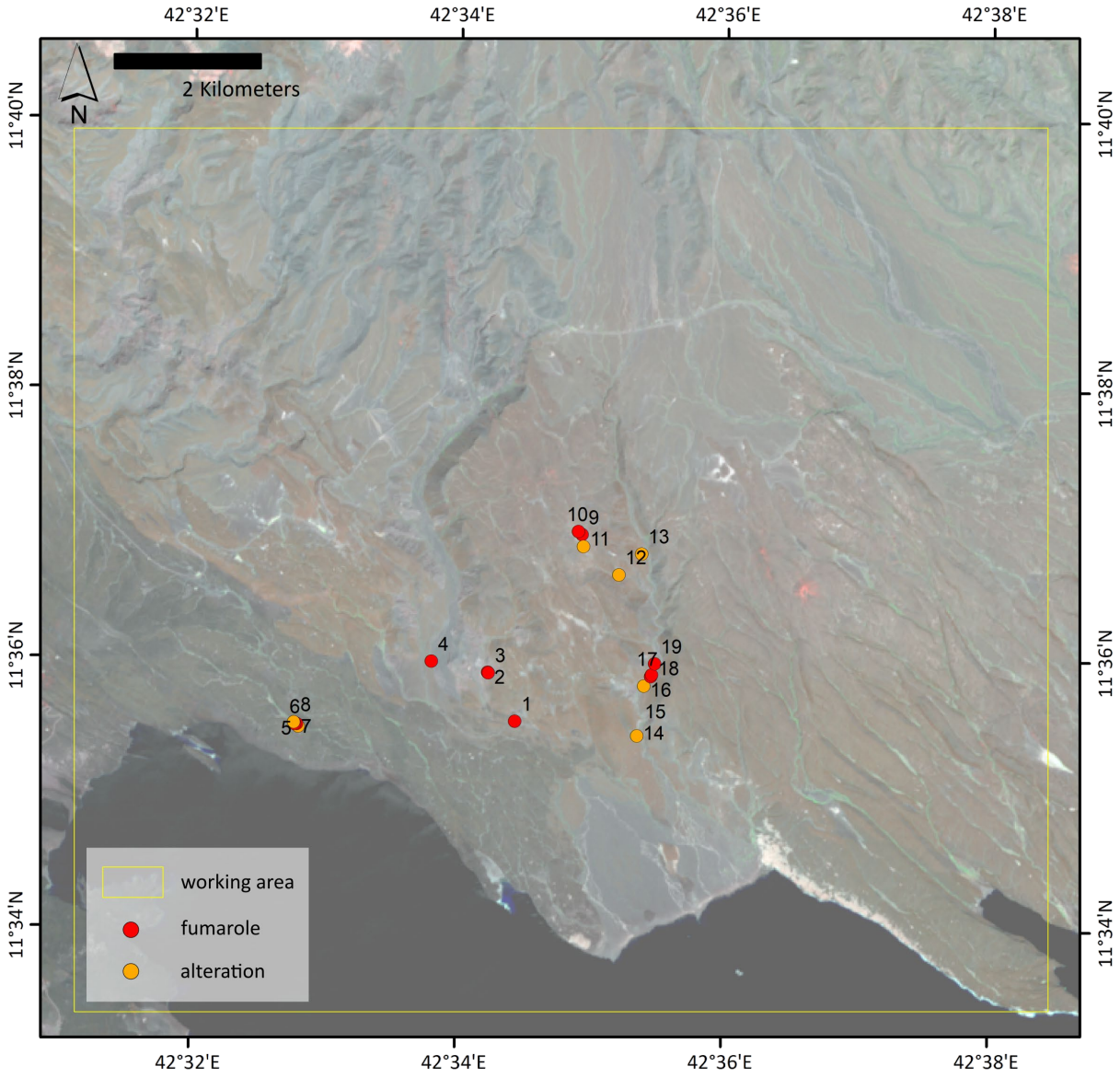
42°32'E
42°34'E
42°36'E
42°38'E
11°40'N
11°38'N
11°36'N
11°34'N
2 Kilometers
N
working area
fumarole
alteration
1
2
3
4
5
6
7
8
9
10
11
12
13
14
15
16
17
18
19